# Tau polarization and correlated decays in neutrino experiments

Joshua Isaacson,[1] Stefan Höche,[1] Frank Siegert,[2] and Sherry Wang[3]
[1]*Theory Division, Fermi National Accelerator Laboratory, P.O. Box 500, Batavia, Illinois 60510, USA*
[2]*Institut für Kern- und Teilchenphysik, TU Dresden, 01069 Dresden, Germany*
[3]*Northwestern University, Department of Physics and Astronomy, 2145 Sheridan Road, Evanston, Illinois 60208, USA*

(Received 3 April 2023; accepted 22 September 2023; published 17 November 2023)

We present the first fully differential predictions for tau neutrino scattering in the energy region relevant to the DUNE experiment, including all spin correlations and all tau lepton decay channels. The calculation is performed using a generic interface between the neutrino event generator Achilles and the publicly available, general-purpose collider event simulation framework Sherpa.

DOI: 10.1103/PhysRevD.108.093004

## I. INTRODUCTION

The tau neutrino is commonly considered to be the least well-known elementary particle. The first experimental direct evidence for tau neutrinos was provided about two decades ago by the DONuT experiment [1]. Major limitations on the data set came from a small cross section, the large mass and short lifetime of the tau lepton, and the large irreducible backgrounds. As of today, there are still very few positively identified tau neutrino events from collider based sources, with nine detected by DONuT [2], and ten detected by OPERA [3]. The SuperK [4] and IceCube [5,6] experiments have identified 291 and 1806 tau neutrino candidates from atmospheric and astrophysical sources. New experiments are expected to come online soon, among them DUNE [7,8] and the IceCube upgrade [9], which will improve the precision on the $\nu_\mu \to \nu_\tau$ appearance measurement. These measurements will not have a significant impact on the overall precision on the standard oscillation analyses assuming Standard Model physics [7,10]. However, it is still important to measure this channel as precisely as possible, and constrain both the oscillations and general properties of $\nu_\tau$ interactions on nuclei, since improved constraints can be obtained when including the tau channel [7]. The forward physics facility [11] will use the large forward charm production rate at the LHC to perform precision studies with collider neutrinos, including approximately 10 000 tau neutrinos. Ultra-high-energy neutrino telescopes will set limits on $\nu_\tau$ self-interactions (which are currently unconstrained [12]) and flavor ratios (which are an important observable to constrain new physics [13]). With all of these novel experiments, the tau neutrino data set is expected to grow quickly in the coming years, creating new opportunities for measurements and searches for physics beyond the standard neutrino paradigm [14].

DUNE is especially important to the tau neutrino program, since it will be the only accelerator-based experiment able to collect and accurately reconstruct a sample of oscillated $\nu_\tau$ charged-current (CC) events [15]. DUNE is expected to record approximately 130 $\nu_\tau$ CC events per year in *CP*-optimized neutrino mode, 30 $\bar{\nu}_\tau$ events per year in *CP*-optimized antineutrino mode and about 800 $\nu_\tau$ CC events per year in tau-optimized neutrino mode before the inclusion of efficiency and purity cuts [14]. To make the most of these events, accurate theory predictions are required. Furthermore, considering the staged approach for DUNE, a reduction in systematic uncertainties associated with the theoretical modeling is of even more vital importance. One key observation to help separate the signal from the irreducible background is the fact that the tau is polarized, leading to correlations in the outgoing pions. However, the produced outgoing tau lepton is not fully polarized for DUNE energies [16,17]. Computational tools that model both the intricate aspects of nuclear physics involved in $\nu$-nucleus interactions and the effects of polarized scattering and decay are vital for experimental success [18]. The existing neutrino event generators GENIE [19], NuWro [20], NEUT [21], and GIBUU [22] generate $\nu_\tau$ interactions in the same manner as $\nu_e$ and $\nu_\mu$ events. However, they then assume that the outgoing $\tau$ is purely left-handed and simulate its decay with the help of TAUOLA [23]. We want to note that while TAUOLA can handle polarized $\tau$ decays, the current set of generators do not keep track of the spin information in their interfaces to TAUOLA. We address this shortcoming by constructing an event generator based on a state-of-the art nuclear physics model,

in combination with a general-purpose tau decay simulation including spin correlations between the production and all subsequent decays.

Various theoretical calculations have also addressed nuclear effects on the polarization of the tau in neutrino scattering. However, the previous works either did not include tau decays [16], or they only included the one-body decay of the tau (i.e. $\tau^- \to \nu_\tau \pi^-$) [17]. They demonstrated the dependence of the nuclear effects on the polarization and the impact on observables, respectively. Here, we extend these studies to include all possible decay channels of the tau, while maintaining complete polarization information, and we provide a publicly available simulation package to generate fully differential final states.[1] The calculation is performed using Achilles [24] to handle the nuclear physics effects and Sherpa [25–27] to perform the leptonic calculation and the decay of the tau. This interface extends the one developed in Ref. [28], which also allows to perform the calculation in nearly arbitrary new physics models by means of FeynRules [29,30]. This is therefore the first ever neutrino event generator to appropriately handle the production and decay of the tau leptons, including all possible decays and polarization effects. While the Achilles generator only includes quasielastic scattering, it is important to note that the polarization effects only depend on the momentum of the final-state tau lepton and not the details of the nuclear calculation. However, the cross section is dominated by quasielastic scattering below 5 GeV and resonance scattering between 5 and 7 GeV, while deep inelastic scattering becomes dominant around 10 GeV [31,32]. The DUNE FD tau neutrino flux peaks right near the tau production threshold where quasielastic scattering is the dominant production mechanism.

The outline of this paper is as follows. In Sec. II, we review analytic results on the production and decay of the tau, with a focus on the effects of nuclear physics and the high-energy limit. The implementation of tau decays within the Sherpa framework and the interface between Achilles and Sherpa is described in Sec. III. Comparisons for purely left-handed and the correct polarization is shown for various monochromatic neutrino beam energies as well as for a realistic tau-optimized DUNE neutrino flux in Sec. IV.

## II. POLARIZATION IN TAU LEPTON PRODUCTION AND DECAY

This section provides a brief overview of the main analytic results on the effect of polarization in $\tau$ decays and production. The collinear limit, which provides both theoretical insight and a useful benchmark for the validation of Monte Carlo simulations, is discussed in some detail. Furthermore, the dependency of the polarization of the $\tau$ on the hadronic tensor is reviewed.

### A. Tau decays in the collinear limit

The dominant decay channels of the $\tau$ are into a single pion, leptons, or into a vector-meson resonance. In these channels, ignoring the decays of the vector mesons, the distribution of the final-state momenta can be determined in the collinear limit (i.e. $|\vec{p}_\tau| \to \infty$). These results are useful for the validation of more detailed theoretical predictions.

The rate of the $\tau^\mp \to \pi^\mp \nu_\tau$ decay in the rest frame of the tau is given as [33]

$$\frac{1}{\Gamma_\tau}\frac{d\Gamma_\pi}{d\cos\theta_\pi}(\tau^\mp \to \pi^\mp \nu_\tau) = \frac{1}{2} B_\pi (1 \pm P_\tau \cos\theta_\pi), \quad (1)$$

where $B_\pi$ is the branching fraction of $\tau^\mp \to \pi^\mp \nu_\tau$, $P_\tau$ is the polarization of the $\tau$, and $\theta_\pi$ is the angle between the pion momentum and the tau spin axis, which coincides with the $\tau$ momentum in the lab frame. For a purely right-handed (left-handed) $\tau^-$, the polarization is $P_\tau = +1(-1)$. In terms of the momentum fraction, $x_\pi = E_\pi/E_\tau$, the polar angle is given as

$$\cos\theta_\pi = \frac{2x_\pi - 1 - a^2}{\beta(1-a^2)}, \quad (2)$$

where $a = m_\pi/m_\tau$ and $\beta$ is the velocity of the $\tau$. In the collinear limit, $\beta \to 1$, and making the approximation $a = 0$, one obtains

$$\frac{1}{\Gamma_\tau}\frac{d\Gamma_\pi}{dx_\pi}(\tau^\mp \to \pi^\mp \nu_\tau) = B_\pi (1 \pm P_\tau (2x_\pi - 1)). \quad (3)$$

In this limit, we obtain the prediction for the differential decay rate shown in Fig. 1.

Additionally, for the case of leptonic decays in the collinear and massless limit ($m_e = m_\mu = 0$) the tau decay to leptons is the same for electrons and muons. The differential decay rate is given by [33]

$$\frac{1}{\Gamma_\tau}\frac{d\Gamma_\ell}{dx_\ell}(\tau^\mp \to \ell^\mp \nu_\tau) = \frac{1}{3} B_\ell (1-x_\ell)((5+5x_\ell - 4x_\ell^2) \pm P_\tau (1 + x_\ell - 8x_\ell^2)), \quad (4)$$

where $x_\ell = E_\ell/E_\tau$, and $B_\ell$ is the branching ratio into a given lepton. The rate for leptons is shown in Fig. 1.

Similarly, the decays for the vector-meson decay modes $\tau \to v\nu_\tau$, with $v = \rho$ or $a_1$ were calculated in Ref. [33] and the results are reproduced here for convenience. The mesons are separated into the transverse and longitudinal components in the calculation, since the decays $\rho \to 2\pi$ and $a_1 \to 3\pi$ depend on the polarization of the vector mesons. The angular distribution in the rest frame of the tau is given as

[1]The Achilles version can be found at https://github.com/AchillesGen/Achilles/releases/tag/v0.2.0, and the Sherpa version can be obtained at https://gitlab.com/sherpa-team/sherpa/-/tree/achilles.

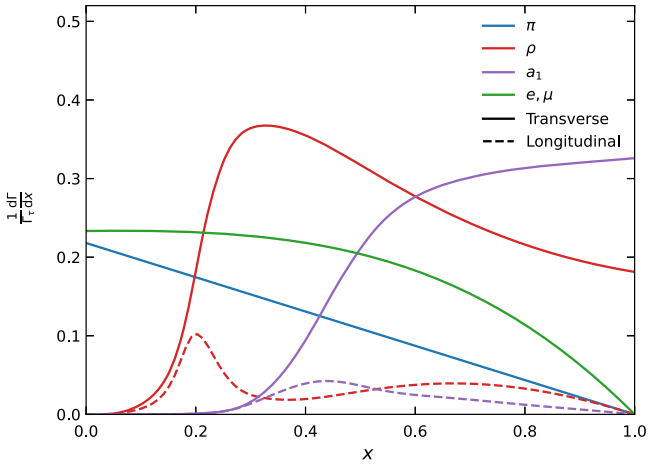


FIG. 1. The decay distributions vs the fractional momentum of a given particle to the $\tau$ momentum for a left-handed $\tau^-$ in the collinear limit going to single pions (blue), $\rho$ mesons (red), $a_1$ mesons (purple), or leptons (green). The vector mesons ($\rho$ and $a_1$) can be either transversely polarized (solid lines) or longitudinally polarized (dashed lines). Additionally, the vector mesons are not stable and the effects of their widths are included, which are set to 0.1474 and 0.420 GeV for the $\rho$ and $a_1$ respectively. The branching ratios are those given in Table I.

$$\frac{1}{\Gamma_\tau}\frac{d\Gamma_v^T}{d\cos\theta_v}(\tau^\mp \to v^\mp \nu_\tau) = B_v \frac{m_v^2}{m_\tau^2 + 2m_v^2}(1 \mp P_\tau \cos\theta_v), \tag{5}$$

$$\frac{1}{\Gamma_\tau}\frac{d\Gamma_v^L}{d\cos\theta_v}(\tau^\mp \to v^\mp \nu_\tau) = B_v \frac{\frac{1}{2}m_v^2}{m_\tau^2 + 2m_v^2}(1 \pm P_\tau \cos\theta_v), \tag{6}$$

where again $v = \rho$ or $a_1$, $B_v$ is the branching ratio for $\tau^\mp \to v^\mp \nu_\tau$, and $\theta_v$ is the same angle defined in the pion case. It is important to note that for the case of the longitudinal state the polarization dependence is the same as Eq. (1), while for the transverse state the polarization enters with the opposite sign. Therefore, if the polarization of the vector meson is not measured, then Eqs. (5) and (6) need to be averaged. This suppresses the sensitivity to the polarization of the tau by a factor of $(m_\tau^2 - 2m_v^2)/(m_\tau^2 + 2m_v^2)$, which is about 0.46 for the case of the $\rho$ and approximately 0.02 for the case of the $a_1$ meson.

In the case of the vector mesons, care has to be taken when boosting to the lab frame since the polarizations are not summed over. First, a Wigner rotation [34] is used to align the spin axis. The angle of rotation is given in the collinear limit by [33]

$$\cos\omega = \frac{1 - a^2 + (1 + a^2)\cos\theta}{1 + a^2 + (1 - a^2)\cos\theta}, \tag{7}$$

where $a = m_v/m_\tau$. Rewriting in terms of the momentum fraction ($x_v = E_v/E_\tau$), the decay distributions can be expressed as

$$\frac{1}{\Gamma_\tau}\frac{d\Gamma_v}{dx_v} = B_v H_v^\alpha(x_v, m_v^2), \tag{8}$$

where $\alpha = T$ or $L$ and the expressions for $H_v^{T,L}$ are given in Eqs. (2.16) and (2.17) of Ref. [33] respectively. The results for the decay distribution including the width for a left-handed $\tau^-$ decay are shown in Fig. 1. These distributions provide the main analytic benchmark points for tests of our Monte Carlo implementation.

### B. Production of the tau lepton

The unpolarized differential cross section for the CC interaction $\nu_\tau A \to \tau^- X$ can be expressed as the product of a leptonic and hadronic tensor as shown in Ref. [28]. In the case of a massive lepton, there are six nuclear structure functions that appear in the hadronic tensor with an associated Lorentz structure [17]

$$\frac{W^{\mu\nu}}{2M_A} = -g^{\mu\nu}W_1 + \frac{P^\mu P^\nu}{M_A^2}W_2 + i\frac{\epsilon^{\mu\nu\gamma\delta}P_\gamma q_\delta}{2M_A^2}W_3 + \frac{q^\mu q^\nu}{M_A^2}W_4 + \frac{P^\mu q^\nu + P^\nu q^\mu}{2M_A^2}W_5 + i\frac{P^\mu q^\nu - P^\nu q^\mu}{2M_A^2}W_6, \tag{9}$$

where $M_A$ is the mass of the nucleus, $P^\mu$ is the initial momentum of the nucleus, $q^\mu$ is the momentum transfer, and $\epsilon^{\mu\nu\gamma\delta}$ is the fully antisymmetric tensor with $\epsilon^{0123} = +1$.

The unpolarized, longitudinal, and transverse components for the production of the $\tau$ can be expressed as different linear combinations of the hadronic structure functions, $W_i$. These are given in Eqs. (2), (5), and (6) of Ref. [35] and are reproduced here for completeness:

$$F = \left(2W_1 + \frac{m_l^2}{M_A^2}W_4\right)(E_l - |\vec{p}_l|\cos\theta) + W_2(E_l + |\vec{p}_l|\cos\theta) - W_5\frac{m_l^2}{M_A} \mp \frac{W_3}{M_A}(E_\nu E_l + |\vec{p}_l|^2 - (E_\nu + E_l)|\vec{p}_l|\cos\theta), \tag{10}$$

$$P_L = \mp\left(\left(2W_1 - \frac{m_l^2}{M_A^2}W_4\right)(|\vec{p}_l| - E_l\cos\theta) + W_2(|\vec{p}_l| + E_l\cos\theta) - W_5\frac{m_l^2}{M_A}\cos\theta \mp \frac{W_3}{M_A}((E_\nu + E_l)|\vec{p}_l| - (E_\nu E_l + |\vec{p}_l|^2)\cos\theta)\right)/F, \tag{11}$$

$$P_T = \mp m_l \sin\theta \left( 2W_1 - W_2 - \frac{m_l^2}{M_A^2} W_4 + W_5 \frac{E_l}{M_A} \mp W_3 \frac{E_\nu}{M_A} \right) / F, \quad (12)$$

where $E_l, m_l, \vec{p}_l$ are the outgoing lepton energy, mass, and three-momentum, respectively. Additionally, $\theta$ is the outgoing lepton angle with respect to the neutrino direction and $E_\nu$ is the energy of the incoming neutrino. It is important to note that the above equations are insensitive to the $W_6$ structure function. Furthermore, the structure functions $W_4$ and $W_5$ are proportional to the mass of the lepton and are only weakly constrained due to the limited statistics on tau-neutrino-nucleus scattering. The combination of both inclusive, differential rates, and polarization information would provide valuable constraints on nuclear models used to describe neutrino-nucleus interactions due to the different set of linear combinations of structure functions that arise in each observable [17]. Additionally, DUNE will be the first experiment to provide measurements of the $W_4$ and $W_5$ structure functions in the quasielastic region, directly testing the partially conserved axial current and the pion-pole dominance ansatz [14].

## III. MONTE CARLO SIMULATION

In this section we review our approach to the simulation of the scattering and decay processes. We make use of the fact that the reaction factorizes into a leptonic and a hadronic component. We employ the neutrino event generator Achilles [24] to handle the nuclear physics effects and the general-purpose event-generation framework Sherpa [25–27] to perform the leptonic calculation and the decay of the tau. The Sherpa framework includes two modules to simulate decays of unstable particles: one for prompt decays of particles produced in the hard scattering process perturbatively, and one for the decay of hadrons produced during the hadronization stage of event generation. The tau lepton plays a special role, as it can be produced in the hard scattering process, but is the only lepton that can decay into hadrons. For a good modeling of tau decays and also for the hadronic decay modes we thus employ the hadron decay module [36,37]. It enables us to use elaborate form factor models, accurate branching fractions for individual hadronic final states, and spin correlation effects for the decaying tau lepton. We briefly describe these features in the following.

### A. The decay cascade

With the observed tau decay channels by the Particle Data Group [38] accounting for roughly 100% of the tau width, we use these values directly for the simulation by choosing a decay channel according to the measured branching fractions. This can include fully leptonic decay channels as well as decays into up to six hadrons.

Matrix elements are used to simulate the kinematical distribution of the decay in phase space. In the case of weak tau decays, these matrix elements will always contain a leptonic current $L_\mu^{(\tau\to\nu_\tau)}$ involving the $\tau$ and $\nu_\tau$ leptons, and a second current involving either another lepton pair or hadronic decay products. Due to the low tau mass and the low related momentum transfer $Q^2 \ll m_W^2$, the $W$ propagator between these currents can be integrated out into the Fermi constant

$$\mathcal{M} = \frac{G_F}{\sqrt{2}} L_\mu^{(\tau\to\nu_\tau)} J^\mu. \quad (13)$$

For currents $J^\mu$ involving hadronic final states, these matrix elements cannot be derived from first principles, but are instead based on the spin of the involved particles and include form factors to account for bound-state effects and hadronic resonances within the hadronic current in particular.

### B. Form factor models in hadronic currents

While the current for the production of a single meson is trivial and determined fully by the meson's decay constant, the currents in multiple-meson production can contain resonance structures. For example, in the production of pions and kaons the main effects stem from intermediate vector mesons with a short lifetime, like $\rho$ or $K^*$. In the Sherpa simulation, the currents are thus supplemented with form factors that parametrize these effects using one of two approaches [36]. Below we highlight these two different approaches currently implemented in Sherpa.

The Kühn-Santamaria (KS) model [39] is a relatively simple approach modeling resonances based on their Breit-Wigner distribution. Multiple resonances can contribute to the same current and are weighted with parameters that are fit to experimental data. The width in the Breit-Wigner distribution is calculated as a function of the momentum transfer.

Another approach for the form factor is based on resonance chiral theory [40], an extension of chiral perturbation theory to higher energies where resonances become relevant. Also here an energy-dependent width is used for the implementation of the resonances. This form factor model is superior for final states dominated by one resonance but cannot model multiple resonances. It will thus yield significant differences with respect to the KS model for any channel where the lower-lying resonances are kinematically suppressed, e.g. two-kaon production.

### C. Spin correlations

The implementation of spin correlations in the Monte Carlo simulation of particle decays was described

in detail in Ref. [41]. This algorithm uses spin-density matrices to properly track polarization information through the decays. Here we summarize only its main features. First, the matrix element is evaluated for all possible spin states for the initial and final states ($\mathcal{M}_{\kappa_1\kappa_2;\lambda_1\ldots\lambda_n}$), where $\kappa_i$ is the spin of the $i$th incoming particle and $\lambda_j$ is the spin of the $j$th outgoing particle in a $2 \to n$ scattering process. The matrix element squared involved in the calculation of the differential cross section can be obtained as

$$\rho^1_{\kappa_1\kappa_1'}\rho^2_{\kappa_2\kappa_2'}\mathcal{M}_{\kappa_1\kappa_2;\lambda_1\ldots\lambda_n}\mathcal{M}^*_{\kappa_1'\kappa_2';\lambda_1'\ldots\lambda_n'}\prod_{i=1,n}D^i_{\lambda_i\lambda_i'}, \tag{14}$$

where $\rho^i_{\kappa_i\kappa_i'}$ is the spin-density matrix for the incoming particles and $D^i_{\lambda_i\lambda_i'}$ is the spin-dependent decay matrix for the outgoing particles. Before any decays occur, the decay matrix is given as $D^i_{\lambda_i\lambda_i'} = \delta_{\lambda_i\lambda_i'}$ and the spin-density matrix is given as $\rho^i_{\kappa_i\kappa_i'} = \frac{1}{2}\delta_{\kappa_i\kappa_i'}$ for unpolarized incoming particles. Second, one of the unstable final-state particles is selected at random to decay and the spin-density matrix is calculated as

$$\rho_{\lambda_j\lambda_j'} = \frac{1}{N_p}\rho^1_{\kappa_1\kappa_1'}\rho^2_{\kappa_2\kappa_2'}\mathcal{M}_{\kappa_1\kappa_2;\lambda_1\ldots\lambda_n}\mathcal{M}^*_{\kappa_1'\kappa_2';\lambda_1'\ldots\lambda_n'}\prod_{i\neq j}D^i_{\lambda_i\lambda_i'}, \tag{15}$$

where $N_p$ is a normalization factor to ensure that the trace of the spin-density matrix is one. The decay channel is then selected according to the branching ratios and the new particle momenta are generated according to

$$\rho_{\lambda_0\lambda_0'}\mathcal{M}_{\lambda_0;\lambda_1\ldots\lambda_k}\mathcal{M}^*_{\lambda_0';\lambda_1'\ldots\lambda_k'}\prod_{i=1,k}D^i_{\lambda_i\lambda_i'}, \tag{16}$$

where $\lambda_0$ is the helicity of the decaying particle and $\lambda_i$ is the helicity of the decay products. If there are any unstable particles in the above decay, they are selected as before and a spin-density matrix is calculated and the process is repeated until only stable particles remain in the given chain. At this point, the decay matrix is calculated as

$$D_{\lambda_0\lambda_0'} = \frac{1}{N_D}\mathcal{M}_{\lambda_0;\lambda_1\ldots\lambda_k}\mathcal{M}^*_{\lambda_0';\lambda_1'\ldots\lambda_k'}\prod_{i=1,n}D^i_{\lambda_i\lambda_i'}, \tag{17}$$

where $N_D$ is chosen such that the trace of the decay matrix is one. Then another unstable particle is selected from the original decay and the process is repeated until the first decay chain ends in only stable particles. At this point, the next unstable particle is selected in the hard process and the above procedure repeats. Once there are only stable particles left, the procedure terminates.

### D. Achilles-Sherpa interface

Employing a dedicated version of the general-purpose event generator Sherpa [25–27], we construct an interface to the Comix matrix element generator [42] to extract the leptonic current. This interface has been described in detail in Ref. [28]. In order to provide the hard scattering amplitudes, $\mathcal{M}_{\kappa_1\kappa_2;\lambda_1\ldots\lambda_n}$, needed for the spin correlation algorithm in Sec. III C, we make use of the methods developed in Ref. [43]. This allows us to extract a spin-dependent leptonic current from Comix, which can be contracted with the hadronic current obtained from Achilles. Schematically this can be written as

$$\mathcal{M}_{\kappa_h\kappa_\nu;\lambda_h\lambda_l\ldots\lambda_n} = g_{\mu\nu}\sum_i L^{(i)\mu}_{\kappa_\nu;\lambda_l\ldots\lambda_n}W^{(i)\nu}_{\kappa_h;\lambda_h}, \tag{18}$$

where we have extended the notation of Ref. [28] to include spin labels. As the spin states of the initial- and final-state hadrons are not observed experimentally, they can be averaged and summed over, leading to the final expression

$$\begin{aligned}&\mathcal{M}_{\kappa_\nu;\lambda_l\ldots\lambda_n}\mathcal{M}^*_{\kappa_\nu';\lambda_l'\ldots\lambda_n'}\\ &= \frac{1}{2}g_{\mu\nu}g_{\mu'\nu'}\sum_{i,i'}L^{(i)\mu}_{\kappa_\nu;\lambda_l\ldots\lambda_n}L^{(i')\mu'}_{\kappa_\nu';\lambda_l'\ldots\lambda_n'}W^{(i)\nu}_{\kappa_h;\lambda_h}W^{(i')\nu'}_{\kappa_h';\lambda_h'}\delta_{\kappa_h\kappa_h'}\delta_{\lambda_h\lambda_h'}.\end{aligned} \tag{19}$$

The resulting tensor is inserted into the event record of Sherpa and used to seed the event-generation algorithms described in Refs. [36,43], which accounts for all spin correlations along all decay chains. We note that this procedure is independent of the physics model for the short-distance interactions, and that arbitrary beyond-Standard-Model scenarios can easily be implemented by providing the corresponding UFO output [44] of FeynRules [29,30].

## IV. RESULTS

We consider the scattering of a tau neutrino off an argon nucleus through the use of a rescaled carbon spectral function for both a monochromatic beam (for validation) and for a realistic flux at DUNE. For this study, we focus only on the quasielastic region for the nuclear interaction, as implemented in Ref. [24], and we neglect final-state interactions. When considering only hadronic decays of the tau, final-state interactions will modify the two- and three-pion distributions. This modification is due to the fact that pions can be produced by final-state interactions. However, the tau will decay outside the nucleus and therefore would not modify the single-pion channel. Investigating the size of the changes is left to a future work. The analysis of the events is performed using Rivet [45,46].[2] For reference, all

[2]The analysis code can be downloaded from [47].

TABLE I. Decay channels of the tau lepton with branching fractions greater than 0.5%. All other channels are grouped into the "other" category.

| Decay mode | Branching ratio (%) |
|---|---|
| Leptonic decays | 35.21 |
| $e^-\nu_\tau\bar{\nu}_e$ | 17.85 |
| $\mu^-\nu_\tau\bar{\nu}_\mu$ | 17.36 |
| Hadronic decays | 64.79 |
| $\pi^-\pi^0\nu_\tau$ | 25.50 |
| $\pi^-\nu_\tau$ | 10.90 |
| $\pi^+\pi^-\pi^-\nu_\tau$ | 9.32 |
| $\pi^-\pi^0\pi^0\nu_\tau$ | 9.17 |
| $\pi^+\pi^-\pi^-\pi^0\nu_\tau$ | 4.50 |
| $\pi^-\pi^0\pi^0\pi^0\nu_\tau$ | 1.04 |
| $K^-\nu_\tau$ | 0.70 |
| $\pi^+\pi^-\pi^-\pi^0\pi^0$ | 0.55 |
| Other | 3.11 |

tau lepton decay channels with a branching ratio above 0.5% are given in Table I. However, all possible decays are actually included in our simulation.

The spectral function used in this calculation was obtained within the correlated basis function theory of Ref. [48]. Electron scattering data is used to constrain the low-momentum and low-energy contributions in the mean-field calculations. The correlated component is obtained within the local density approximation. The normalization of the spectral function is taken as

$$\int \frac{\mathrm{d}k_h}{(2\pi)^3}\mathrm{d}E S_h(\vec{k}_h, E) = \begin{cases} Z, & h = p, \\ A - Z, & h = n, \end{cases} \tag{20}$$

where $k_h$ is the momentum of the initial nucleon, $E$ is the removal energy, $S_h$ is the spectral function, and $Z(A)$ denotes the number of protons (nucleons) in the nucleus.

In this work, we consider the Kelly parametrization for the electric and magnetic form factors [49], and use a dipole axial form factor with $g_A = 1.2694$ and $M_A = 1.0$ GeV. Additionally, the pseudoscalar form factor is obtained through the use of the partially conserved axial current ansatz and assumptions about the pion-pole dominance, i.e.

$$F_P^A(Q^2) = \frac{2m_N^2}{Q^2 + m_\pi^2} F^A(Q^2), \tag{21}$$

where $F_P^A$ is the pseudoscalar axial form factor, $m_N$, $m_\pi$ are the masses of the nucleon and pion, respectively, $Q^2 = -q^2$ is the four-momentum transfer, and $F^A$ is the axial form factor.

### A. Monochromatic beam

In order to validate our results, we first consider monochromatic beams. We compare our calculations to the results from Ref. [17] for the single-pion production channel. In that work, the authors looked at beam energies of 3, 4, 6, and 10 GeV. We consider the same energies. While the traditional threshold for tau production is considered to be a beam energy of 3.4 GeV, this does not take into account the initial momentum of the neutron in the nucleus. Appendix A evaluates the threshold for tau production while taking into account Fermi motion and the binding energy of the nucleus. However, instead of the momentum of the outgoing pion, we analyze the momentum fraction of the outgoing pion ($x_\pi = |\vec{p}_\pi|/|\vec{p}_\tau|$). This allows us to include multiple neutrino energies in the same plot. The results from Achilles + Sherpa are shown in Fig. 2, with the appropriate handling of the tau polarization on the left and assuming the tau to be purely left-handed on the right. From this, we see that our results are consistent with those from Ref. [17]. Additionally, we see that as the neutrino energy increases the results approach those found in Fig. 1 for the collinear limit, as expected.

We next consider the decays of the tau into the two-pion and three-pion states, which are dominated by the decay chains $\tau^- \to \nu_\tau \rho^-(\rho^- \to \pi^-\pi^0)$ and $\tau^- \to \nu_\tau a_1^-(a_1^- \to \pi^-\pi^-\pi^+$ or $a_1^- \to \pi^-\pi^0\pi^0)$ respectively.

For the case of the $\rho$ channel, we analyze the momentum fraction of the hadronic system ($x_\rho = |\vec{p}_\rho|/|\vec{p}_\tau|$) as

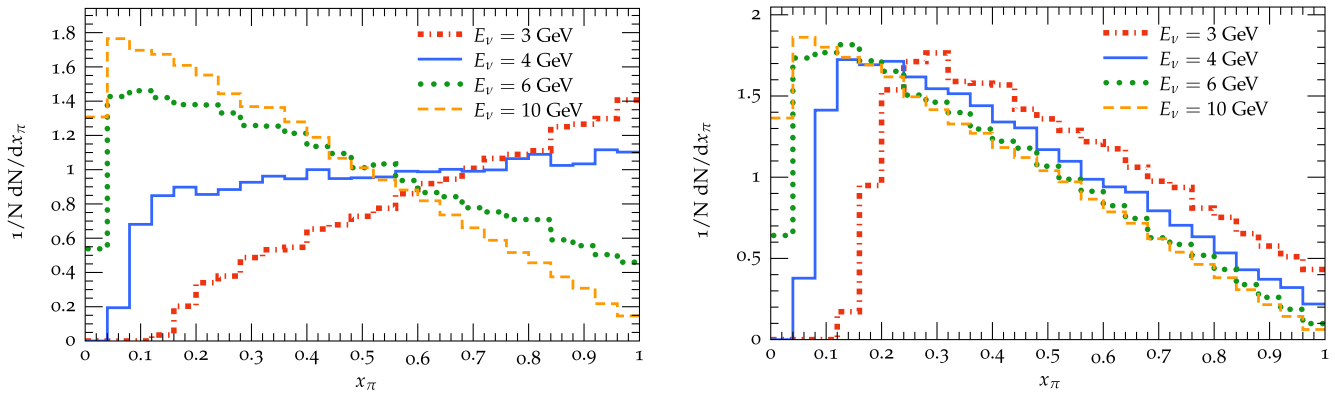


FIG. 2. Momentum fraction of the outgoing pion for $\tau^- \to \pi^-\nu_\tau$ decays of various incoming neutrino energies. Results are shown for the full polarization calculation on the left and the left-handed polarization approximation ($P_L^T = 1, P_T^T = 0$) on the right.

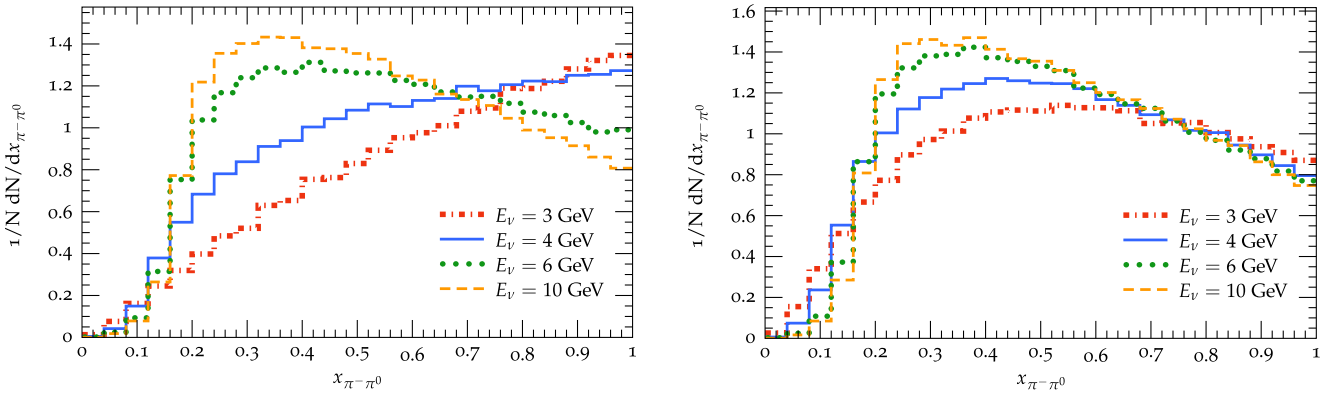


FIG. 3. Momentum fraction of the $\pi^-\pi^0$ system for $\tau^- \to \pi^-\pi^0\nu_\tau$ decays of various incoming neutrino energies. Results are shown for the full polarization calculation on the left and the left-handed polarization approximation ($P_L^T = 1, P_T^T = 0$) on the right.

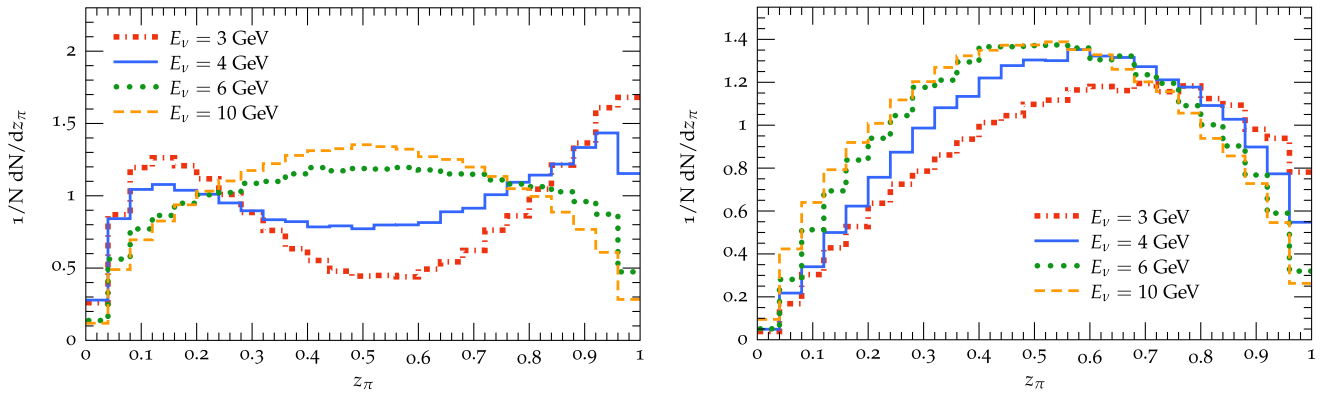


FIG. 4. Ratio of the $\pi^-$ momentum to the $\rho^-$ momentum for $\tau^- \to \pi^-\pi^0\nu_\tau$ decays of various incoming neutrino energies, where $z_\pi$ denotes this ratio. Results are shown for the full polarization calculation on the left and the left-handed polarization approximation ($P_L^T = 1, P_T^T = 0$) on the right.

well as the momentum fraction of the $\pi^-$ with respect to the $\rho$ ($z_\pi = |\vec{p}_{\pi^-}|/|\vec{p}_\rho|$). The results are shown in Figs. 3 and 4 respectively. Again, the full calculation is on the left of each plot and the assumption of a purely left-handed tau is on the right. We can see that there is a significant impact from including the correct polarization in the calculation. In the case of the $\rho$ momentum fraction, we see that our results approach the transverse curve for the $\rho$ from Fig. 1 as $E_\nu$ increases. This is expected since we are summing over the polarizations of the $\rho$, which are dominated by the transverse polarization.

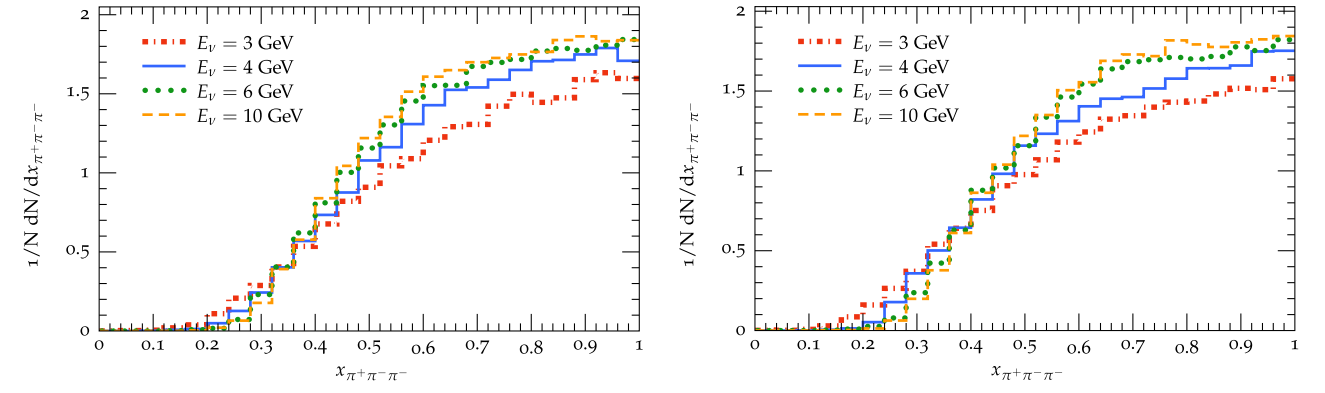


FIG. 5. Momentum fraction of the $\pi^+\pi^-\pi^-$ system for $\tau^- \to \pi^+\pi^-\pi^-\nu_\tau$ decays of various incoming neutrino energies. Results are shown for the full polarization calculation on the left and the left-handed polarization approximation ($P_L^T = 1, P_T^T = 0$) on the right.

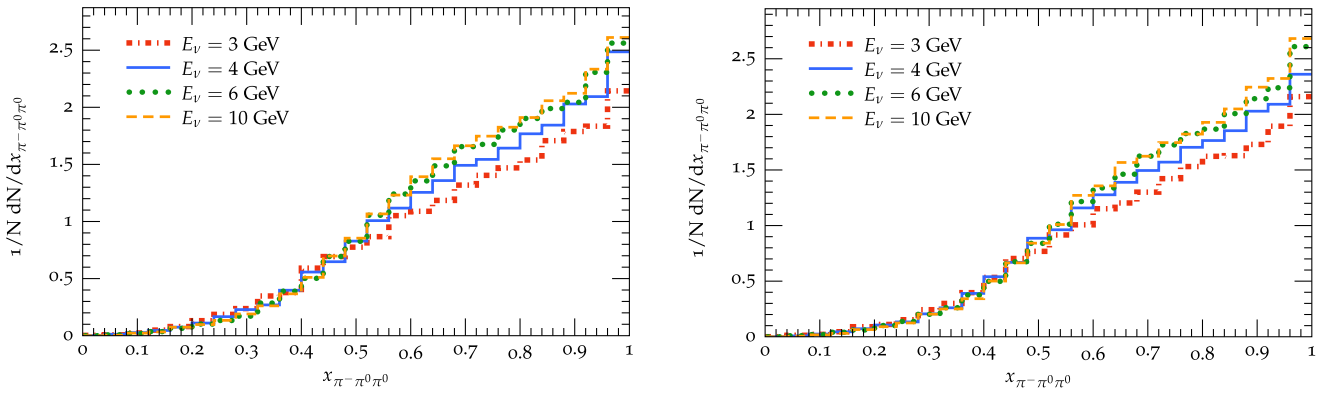


FIG. 6. Momentum fraction of the $\pi^-\pi^0\pi^0$ system for $\tau^- \to \pi^-\pi^0\pi^0\nu_\tau$ decays of various incoming neutrino energies. Results are shown for the full polarization calculation on the left and the left-handed polarization approximation ($P_L^T = 1, P_T^T = 0$) on the right.

As mentioned in Sec. II A, summing over the polarizations of the $a_1$ removes any sensitivity to the polarization of the $\tau$. Therefore, the $a_1$ momentum as a fraction of the $\tau$ momentum ($x_{a_1} = |\vec{p}_{a_1}|/|\vec{p}_\tau|$) should not show any difference between the full calculation and the left-handed only calculation. This is supported by Figs. 5 and 6, with the left and right panels being statistically consistent with each other. Figure 5 shows the decay to the $\pi^+\pi^-\pi^-$ final state and Fig. 6 shows the decay to the $\pi^-\pi^0\pi^0$ final state. Furthermore, the curves approach the result of the collinear limit as $E_\nu$ increases, as seen by comparing to the transverse $a_1$ curve of Fig. 1.

Finally, we consider the leptonic decay channel. Here we focus on the decays to electrons due to the possible experimental relevance at DUNE for $\nu_\tau$ detection, but note that up to corrections from the muon mass and the difference in the branching ratios the predictions would be identical. The comparison for various neutrino energies is given in Fig. 7. Again, we can see a difference between the full calculation in the left panel and the purely left-handed calculation in the right panel. The latter result approaches the expected prediction for large $E_\nu$ as shown in Fig. 1.

### B. Realistic beams

To investigate the impact of spin correlations in a more realistic setting, we consider the $\tau$-optimized flux mode for the DUNE experiment [8,50]. While DUNE will also have a significant number of events from atmospheric neutrinos, the impact of correctly modeling the tau polarization will be negligible due to the significantly higher-energy neutrinos involved. The oscillated far detector flux is shown in Fig. 8. The oscillation parameters are fixed to the values from the global fit [51]:

$$\Delta m^2_{21} = 7.50 \times 10^{-5}\ \text{eV}^2, \qquad \Delta m^2_{31} = 2.55 \times 10^{-3}\ \text{eV}^2,$$
$$\sin^2_{12} = 0.318, \qquad \sin^2_{23} = 0.574, \qquad \sin^2_{13} = 0.0220, \qquad \delta_{CP} = 1.08\pi.$$

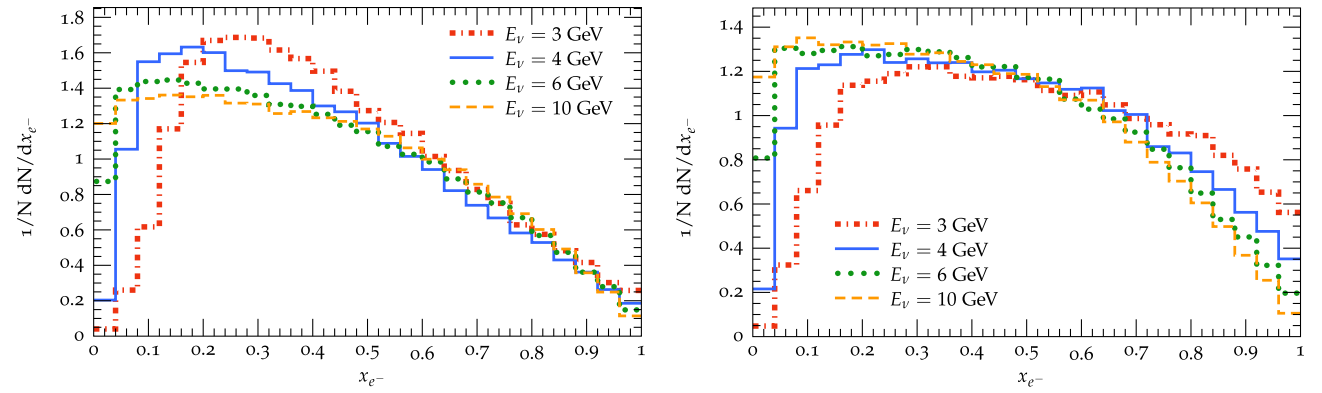


FIG. 7. Momentum fraction of the outgoing electron for $\tau^- \to e^-\nu_\tau\bar{\nu}_e$ decays of various incoming neutrino energies. Results are shown for the full polarization calculation on the left and the left-handed polarization approximation ($P_L^T = 1, P_T^T = 0$) on the right.

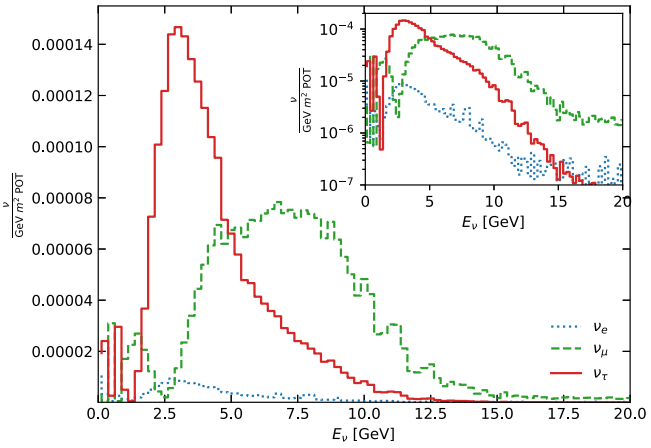


FIG. 8. Neutrino flux in the far detector of DUNE. The flux is generated from running in $\tau$-optimized mode. The unoscillated fluxes are obtained from Refs. [8,50].

The results are given using the flux-averaged cross section, defined as

$$\langle\sigma\rangle = \frac{\int dE_\nu \Phi(E_\nu)\sigma(E_\nu)}{\int dE_\nu \Phi(E_\nu)}, \tag{22}$$

where $\Phi(E_\nu)$ is the neutrino flux and $\sigma(E_\nu)$ is the neutrino energy dependent cross section.

While all possible decay channels are implemented, we consider here only those most affected by correctly handling polarization. Furthermore, only decay channels with sufficiently large branching ratios such that the differences are experimentally relevant are shown.

We first consider the single-pion decay channel, since it is an easy channel to reconstruct at DUNE and liquid-argon time-projection chambers have a very high charged pion reconstruction efficiency and energy measurement. The results of the calculation are shown in the left panel of

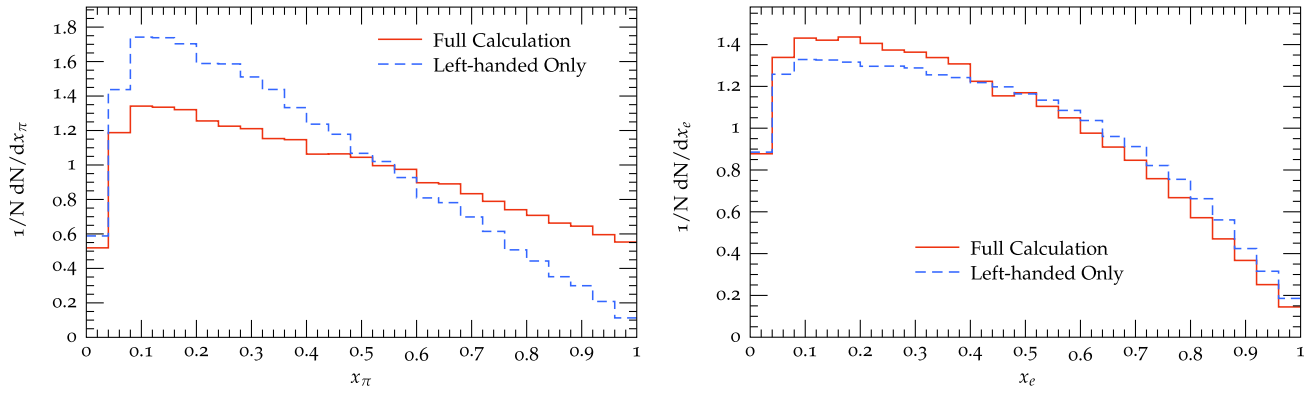


FIG. 9. Momentum fraction distribution for the decay of the $\tau$ into a single pion is shown on the left and momentum fraction distribution for the decay into an electron is shown on the right. The full polarization handling is shown in red with the approximation that the $\tau$ is purely left-handed in blue. The predictions are folded over the DUNE far-detector flux running in the $\tau$-optimized mode given in Fig. 8.

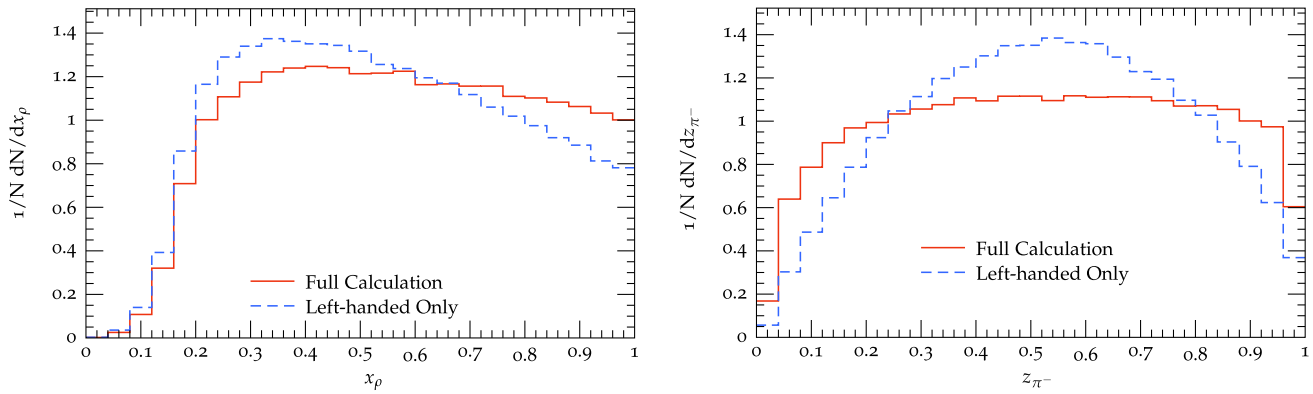


FIG. 10. Momentum fraction distribution for the decay of the $\tau$ into a pair of pions is shown on the left. The momentum of the negatively charged pion as a fraction of the sum of the pion momenta is given on the right. The full polarization handling is shown in red with the approximation that the $\tau$ is purely left-handed in blue. The predictions are folded over the DUNE far-detector flux running in the $\tau$-optimized mode given in Fig. 8.

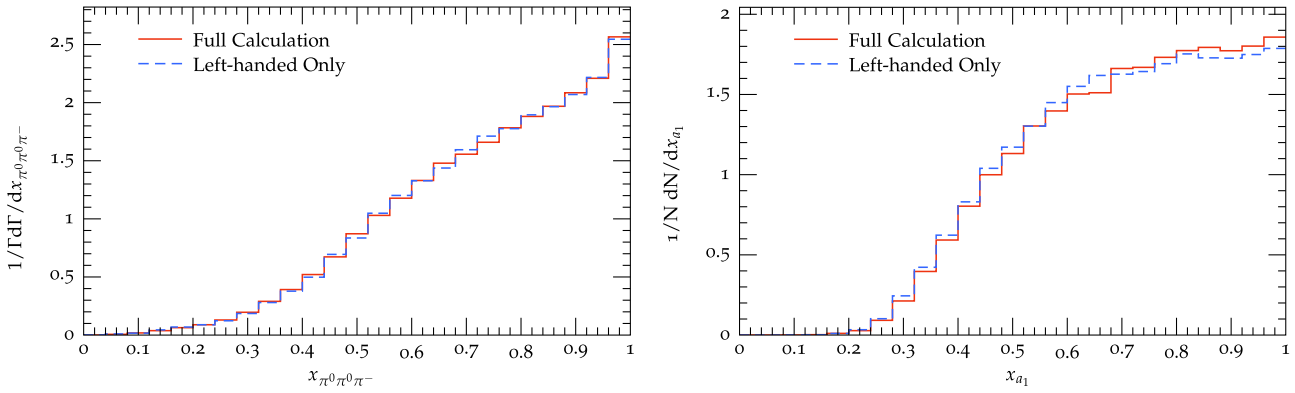


FIG. 11. The full calculation (red) and the purely left-handed calculation (blue) are given for the momentum fraction of the three pions as a fraction of the total $\tau$ momentum for the decay of the $a_1$, with the $\pi^0\pi^0\pi^-$ channel on the left and the $\pi^+\pi^-\pi^-$ channel on the right. The predictions are folded over the DUNE far-detector flux running in the $\tau$-optimized mode given in Fig. 8.

Fig. 9. Here we see that in the full calculation, the outgoing pion tends to be more energetic than in the fully left-handed case.

The case of leptonic decays is shown in the right panel of Fig. 9, and is calculated in the massless limit for both the electron and the muon. In this case, the two decays are identical. The effect of including the full polarization information makes the outgoing lepton softer compared to the fully left-handed calculation. The chance of detecting the muon channel is extremely difficult, due to the large $\nu_\mu$ flux, creating a significant irreducible background from $\nu_\mu$ NC1$\pi$ events, which are indistinguishable from $\nu_\tau$ events. There is a chance to detect the electron channel due to the low $\nu_e$ flux at the far detector as seen in Fig. 8.

Another interesting decay channel to consider is the two-pion final state, which has the largest branching fraction of all decay channels. For this decay channel, we consider the momentum of the sum of the two pions as a fraction of the $\tau$ momentum ($x_{\pi\pi}$) and the momentum of the negatively charged pion as a fraction of the momentum sum ($z_\pi$). Figure 10 shows the difference between the full calculation in red and the fully left-handed approximation in blue. In the case of the $x_{\pi\pi}$ distribution, the total momentum is harder in the full calculation compared to the left-handed assumption. Additionally, there is a significant difference in $z_\pi$ between the full calculation and the left-handed-only calculation. The full calculation is relatively flat over the full range, while the left-handed only calculation is peaked around 0.6. This shift is significant, and will be important for any detailed study using the two-pion channel to detect tau neutrino events.

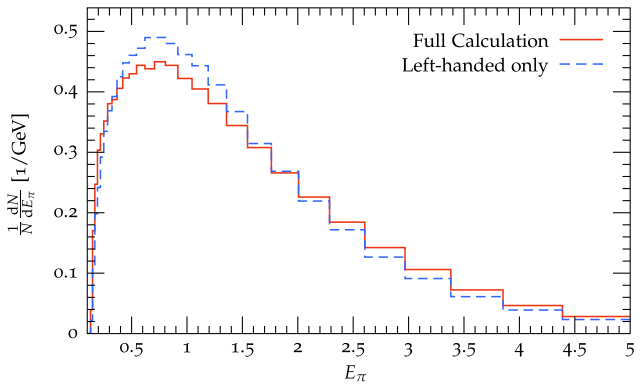


FIG. 12. Energy of the leading pion in $\nu_\tau A \to \tau p(A-1)$ events, in which all possible decays of the $\tau$ are included only considering CCQE events. These results do not include the production of pions from the intranuclear cascade.

The last decay channel considered in this work is the decay to three pions. In this case, the decay is dominated by the $a_1$ meson as discussed in Sec. II A, and since we are not separating out the $a_1$ polarization it should not be sensitive to the polarization of the $\tau$. This can be seen in Fig. 11, where the decay $a_1 \to \pi^0\pi^0\pi^-$ can be seen on the left and the decay $a_1 \to \pi^+\pi^-\pi^-$ can be seen on the right. The full calculation and the left-handed-only calculation are statistically consistent with each other, as expected.

Finally, we perform the analysis proposed in Ref. [18] by considering the energy of the leading pion. The comparison between the full calculation and the left-handed polarization assumption is shown in Fig. 12. There is a shift in the energy distribution of the pion when correctly handling the tau polarization, making the pion slightly harder. The study of the impact of this in the separation from the neutral-current background and other systematic effects is left to a future work. Since the final-state interactions are turned off in this analysis, the other distributions given in Ref. [18] would not be accurate. Therefore, they are not included here but will be included in a detailed study on separating the $\tau$ decays from the background.

## V. CONCLUSIONS

Due to the limited number of identifiable tau neutrino events, the tau neutrino is typically considered the least understood fundamental particle in the Standard Model. Current and next-generation experiments will collect a

large number of tau neutrino events, opening the door to a detailed study of this particle.

One of the most important experiments for studying the tau neutrino will be the DUNE experiment. It will be the only experiment using accelerator neutrinos for measuring properties of the tau neutrino. At DUNE energies, the quasielastic scattering component is the dominant contribution [31]. In this energy region, there is an irreducible background from neutral-current resonance interactions. Therefore, it is vital to understand the most optimal way to separate the signal from the background. Traditionally, in neutrino event generators the outgoing $\tau$ is assumed to be fully left-hand polarized. This assumption is poor for DUNE energies due to the flux being largest near the threshold for $\tau$ production, leading to a significant contribution from right-handed components. Due to the staged approach now planned for DUNE, it becomes vital to perform a dedicated study to investigate the impact proper simulation will have on the overall sensitivity for tau neutrino measurements.

In this work, we demonstrated the appropriate way of calculating the polarization of the tau and propagating this information through the full decay chain within an event-generator framework. The simulations were performed with a publicly available version of Achilles interfaced with Sherpa. While these calculations are only for CC quasielastic (CCQE) and do not include final-state interactions, the overall impact of the tau polarization is controlled by the momentum of the outgoing tau lepton and not the details of the nuclear physics. The final-state interactions may result in shifts in the two- and three-pion distributions due to incorrect pairings for reconstruction of the tau. The size of this effect is left to a future work. For validation, we showed that the distributions for single-pion decays of the tau are consistent with Ref. [17] for monochromatic beams. We additionally showed strong shifts in the momentum distributions for the two-pion decay channel and found insignificant shifts (as expected) in the three-pion decay channels from the fully left-handed assumption. We also considered the decay in the leptonic channel, and found a slight shift when correctly handling the polarization.

While the study with monochromatic beams allows for validation of the calculation, all current and future experiments have a broad spread in the neutrino energies. We therefore investigated the changes in the same distributions integrated over the $\tau$-optimized running mode for DUNE. Again we found significant changes from the traditional fully left-handed assumption in the lepton, single-pion, and two-pion channel. As expected, there were no significant modifications in the three-pion channel.

Finally, while the distributions shown here demonstrate the importance of properly handling the polarization of the tau, they are not necessarily the optimal variables for separating the tau from the neutral-current background. The investigation of how to optimally separate the CC tau neutrino interactions from the Standard Model background is left to a future work.

## ACKNOWLEDGMENTS

We thank Joanna Sobczyk and collaborators for insightful discussions. We thank Noemi Rocco, William Jay, and André de Gouvêa for many useful discussions and for their comments on the manuscript. We thank Pedro Machado for helping with the realistic tau neutrino beams, for many fruitful discussions, and for his comments on the manuscript. This manuscript has been authored by Fermi Research Alliance, LLC under Contract No. DE-AC02-07CH11359 with the U.S. Department of Energy, Office of Science, Office of High Energy Physics.

## APPENDIX A: TAU PRODUCTION THRESHOLD

When calculating events with a massive lepton in the final state, care has to be taken to ensure that there is enough energy to produce the particles. In the case of tau neutrino CC events, the minimum invariant mass of the final-state particles in a CCQE event is given as $s_{\min} = (m_\tau + m_N)^2$, where $m_\tau$ is the tau mass and $m_N$ is the nucleon mass. When considering neutrino scattering on a nucleon within a nucleus, the initial-state momenta are given as

$$p_\nu = \{E_\nu, 0, 0, E_\nu\}, \tag{A1}$$

$$p_N = \{E_N, -p_x, -p_y, -p_z\}, \tag{A2}$$

where we have taken the neutrino of energy $E_\nu$ to be along the $z$ axis, and the nucleon to have an arbitrary momentum with the $z$ component in the opposite direction. Since the nucleon is bound within the nucleus, the on-shell condition ($p_N^2 = m_N^2$) does not hold, and we define the energy to be given as $E_N = m_N - E_b$, where $E_b$ is the binding energy. The minimum neutrino energy required for tau lepton production is thus given by

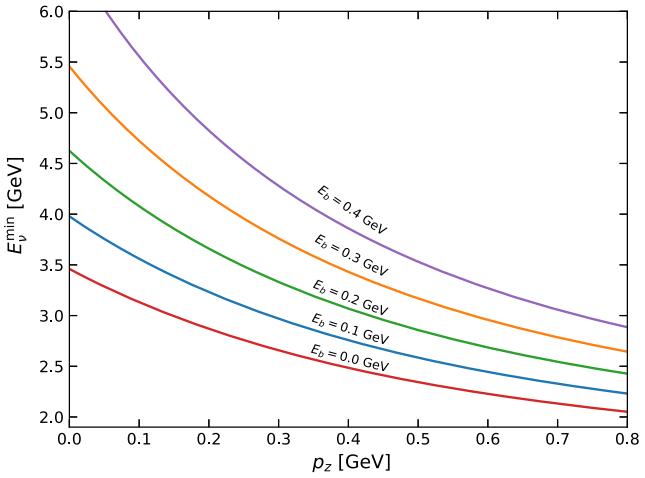


FIG. 13. The minimum required neutrino energy to produce a tau lepton final state as a function of the initial-state nucleon momentum along the neutrino beam direction with with the transverse components set to zero for various binding energies.

$$E_\nu^{\min} = \frac{(m_N + m_\tau)^2 - (E_N^2 - p_x^2 - p_y^2 - p_z^2)}{2(E_N + p_z)}. \quad \text{(A3)}$$

Including the $p_x$ and $p_y$ component will increase the minimum amount of energy required, so to find the absolute threshold we can consider the nucleon to be antiparallel with the neutrino (i.e. $p_x = p_y = 0$). The minimum neutrino energy as a function of $p_z$ is given in Fig. 13 for various binding energies. It is important to note that taking into account the momentum of the initial nucleon decreases the overall threshold to produce tau leptons. However, the contribution to the total rate from this region is significantly phase space suppressed, but nonzero.

## APPENDIX B: ADDITIONAL DISTRIBUTIONS

In the following appendix, we show an additional set of observables that would be more easily measurable experimentally. In this work we only focus on only pion final states. The analysis can be found in Ref. [47], and includes distributions with final states that are not exclusively pions.

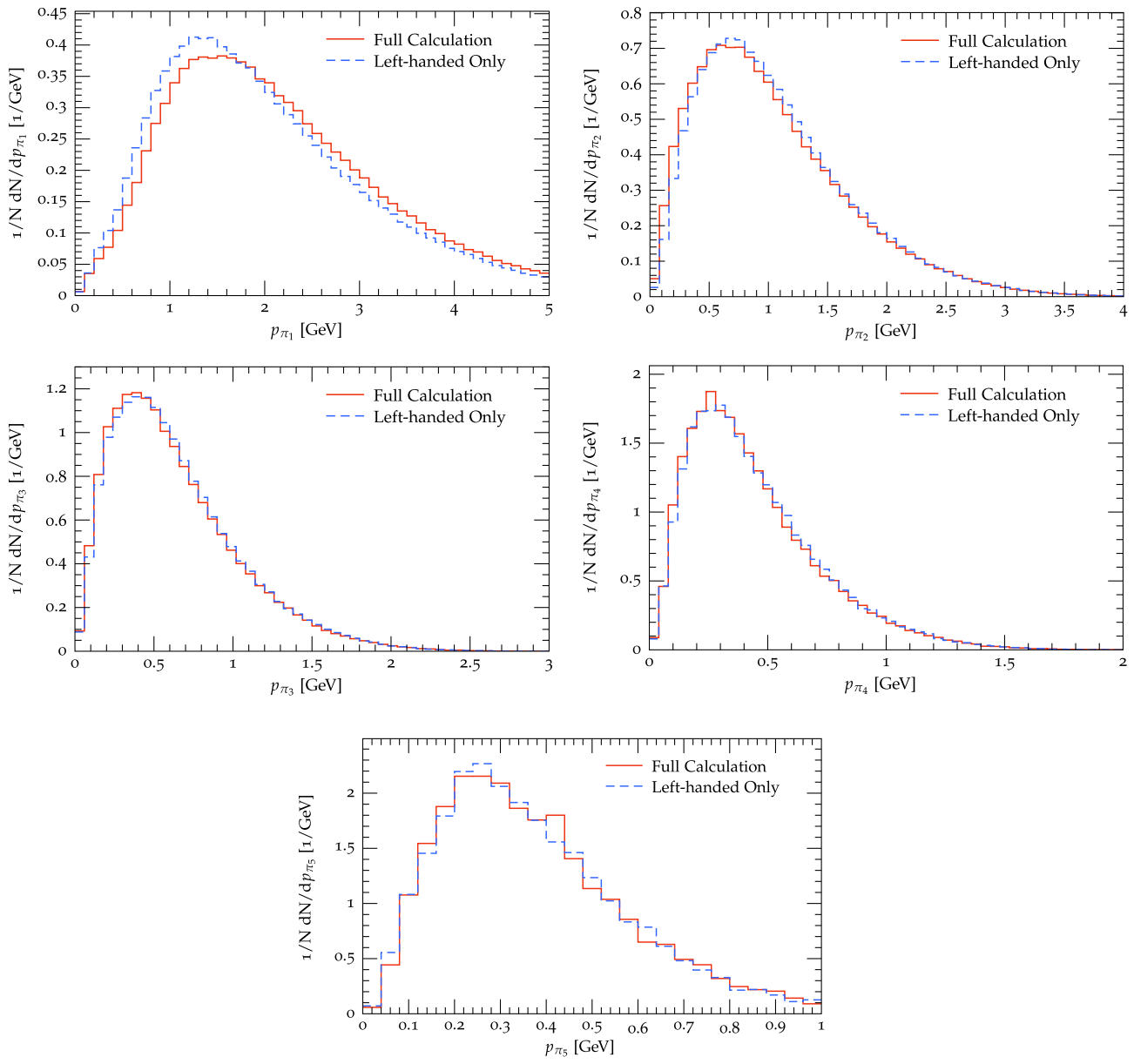


FIG. 14. The momentum of the $n$th most energetic pion. The red curve represents appropriately handling the polarization of the tau, while the blue line represents the assumption of a purely left-handed tau. The upper left plot corresponds to the leading pion, the upper right corresponds to the second most energetic pion, the middle row consists of the third and fourth most energetic pions, and the last row contains the distribution for the fifth most energetic pion.

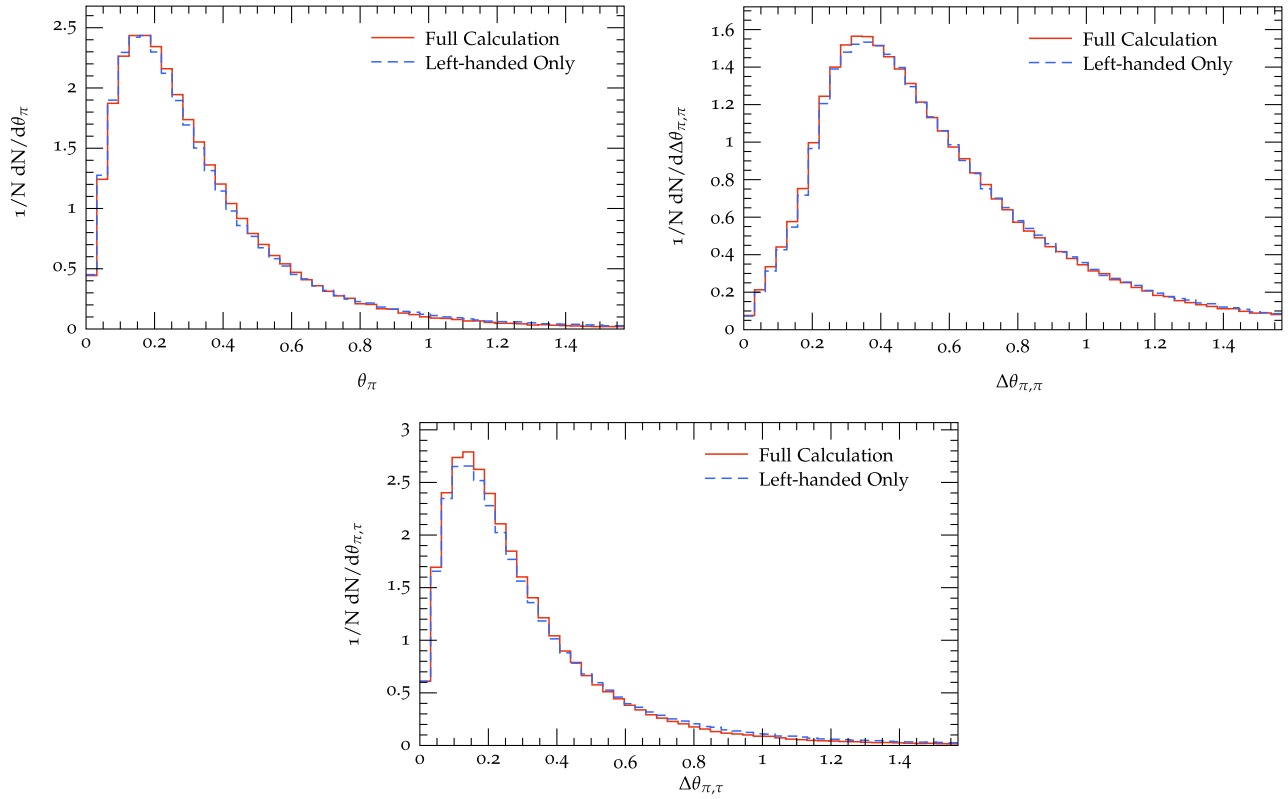


FIG. 15. The upper left plots shows the angle of the most energetic pion with respect to the neutrino beam direction. The upper right plot shows the angle between the leading and subleading pions. The bottom plot shows the angle between the leading pion and the tau lepton. In all the plots, the red curve corresponds to the full calculation taking the polarization into consideration, while the blue curve corresponds to the purely left-handed approximation.

### 1. Inclusive distributions

For the inclusive distributions, we consider all events with at least one pion, including events with other mesons involved such as kaons and etas for example. For these distributions, we include the momentum of the $n$th most energetic pion, shown in Fig. 14. We show the distributions up to the fifth most energetic pion.

In Fig. 14, we see that the effect of including the pion polarization is most important for the leading pion, and becomes less important as we consider less energetic pions.

Additionally, we consider the angle of the most energetic pion with respect to the neutrino beam direction, the angle between the leading and subleading pions, and the angle between the most energetic pion and the tau lepton.

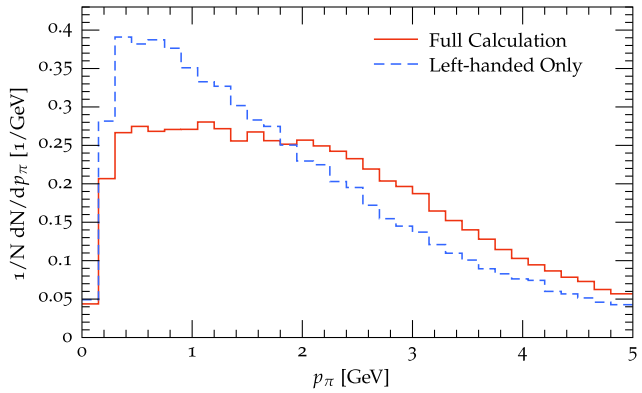


FIG. 16. The distribution of the momentum of the pion for the decay channel $\tau \to \pi\nu_\tau$ is shown. The results with the purely left-handed approximation are given in blue, while the full calculation is given in red.

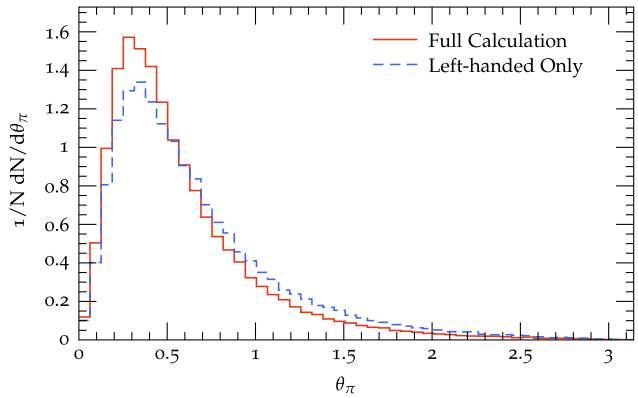


FIG. 17. The distribution of the angle of the pion with respect to the neutrino beam for the decay channel $\tau \to \pi\nu_\tau$ is shown. The results with the purely left-handed approximation are given in blue, while the full calculation is given in red.

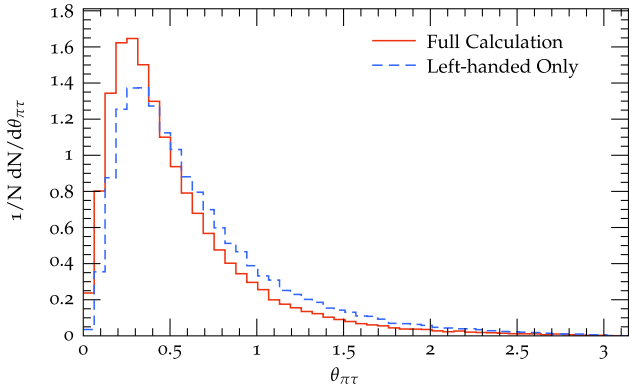


FIG. 18. The distribution of the angle of the pion with respect to the tau lepton for the decay channel $\tau \to \pi\nu_\tau$ is shown. The results with the purely left-handed approximation are given in blue, while the full calculation is given in red.

These results are shown in Fig. 15. In this set of angular distributions, we do not see any strong correlation in how the tau polarization is handled. More complex angular distributions and the impacts on isolating tau events from the backgrounds are left to a future work.

### 2. Single-pion distributions

Next, we consider the case of events with only a pion in the final state, i.e. $\tau \to \pi\nu_\tau$. We investigate a few distributions that can be constructed by showing the impact of properly handling the polarization of the tau. In Fig. 16, the momentum of the single pion is shown. Here we can see a significant difference between the case for the purely left-handed calculation and the full calculation. Additionally, in Figs. 17 and 18, we investigate the effects in the angle of the pion with respect to the neutrino beam and with respect to the tau lepton respectively. In both cases, we see a significant shift from the approximate calculation to the full calculation.

The effects shown here will have important consequences for the performance of DUNE in detecting tau neutrino events. The exact effects require a detailed modeling of the background, along with detector simulation and cuts. Furthermore, it would involve investigating correlations between observables to optimize the selection criteria. Due to these complex factors, this investigation is left to a future work.

### 3. Two-pion distributions

Furthermore, we investigate the case of events with exactly two pions in the final state, i.e. $\tau \to \pi\pi\nu_\tau$. We consider the same set of observables as in the single-pion case plus a few additional observables that can only be constructed with multiple pions. In Fig. 19, the momentum of the leading and subleading pions are shown. Here we can see a significant difference between the case for the purely left-handed calculation and the full calculation for the leading pion, and a less significant impact on the subleading pion. Additionally, in Figs. 20 and 21, we investigate the effects in the angle of the leading pion, subleading pion, and the two-pion system with respect to the neutrino beam and with respect to the tau lepton respectively. In the aforementioned distributions, the left-hand only and the full calculation have negligible differences. Finally, we consider the opening angle between the two pions in Fig. 22, and find no significant impact on the observable from appropriately handling the spin correlations.

Again, the shift in the momentum distributions is significant and will have an impact on the results of DUNE. The exact effect that would result from this shift involves a detailed comparison and additional investigations into the optimal separation of the signal from the background. For these reasons, this is left to a future work.

### 4. Three-pion distributions

Additionally, we investigated the case of events with exactly three pions in the final state, i.e. $\tau \to \pi\pi\pi\nu_\tau$. We consider the same set of observables as in the two-pion case, but with the additional combinations that can be constructed with three pions. In Fig. 23, the momentum of

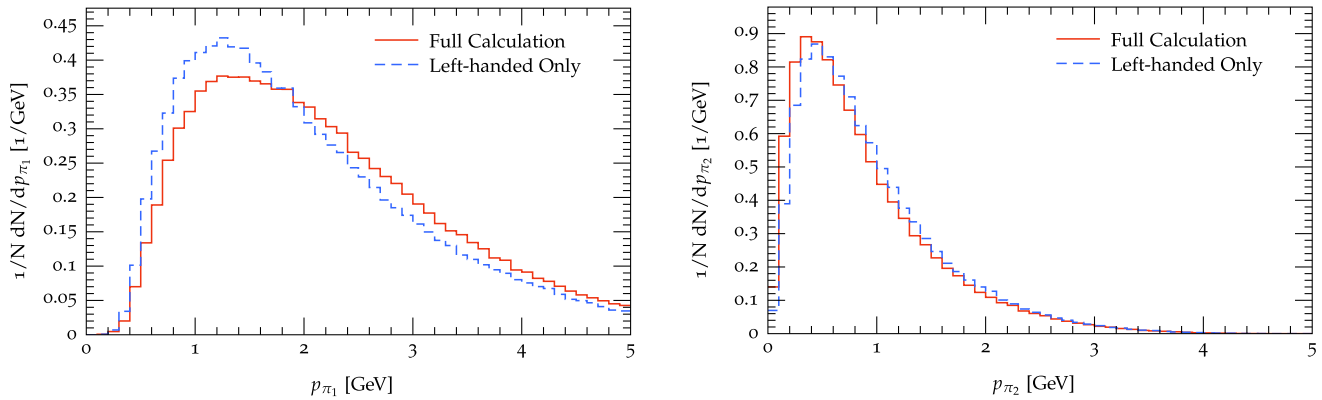


FIG. 19. The distributions of the leading (left) and subleading (right) momentum of the pion for the decay channel $\tau \to \pi\pi\nu_\tau$ are shown. The results with the purely left-handed approximation are given in blue, while the full calculation is given in red.

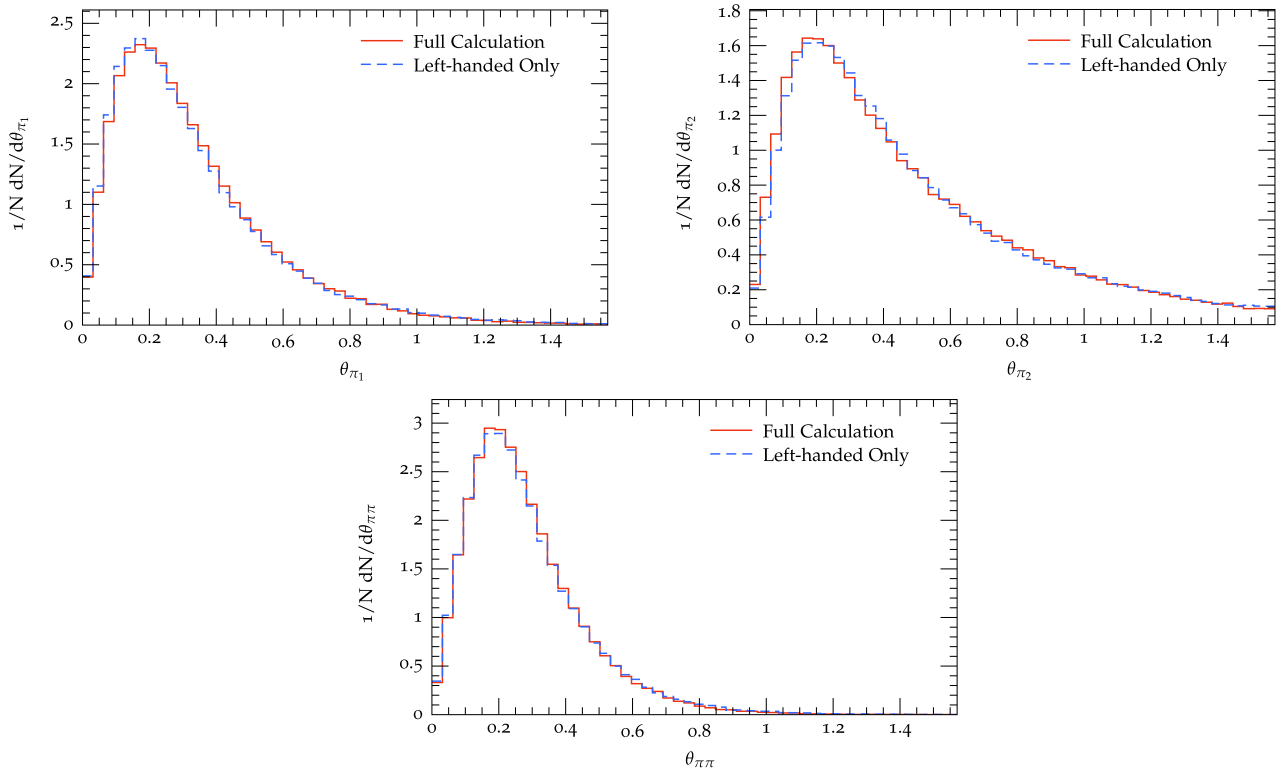


FIG. 20. The distributions of the leading (left) and subleading (right) pion angle with respect to the neutrino beam axis for the decay channel $\tau \to \pi\pi\nu_\tau$ are shown. Additionally, the angle between the two pions and the neutrino beam is shown in the bottom. The results with the purely left-handed approximation are given in blue, while the full calculation is given in red.

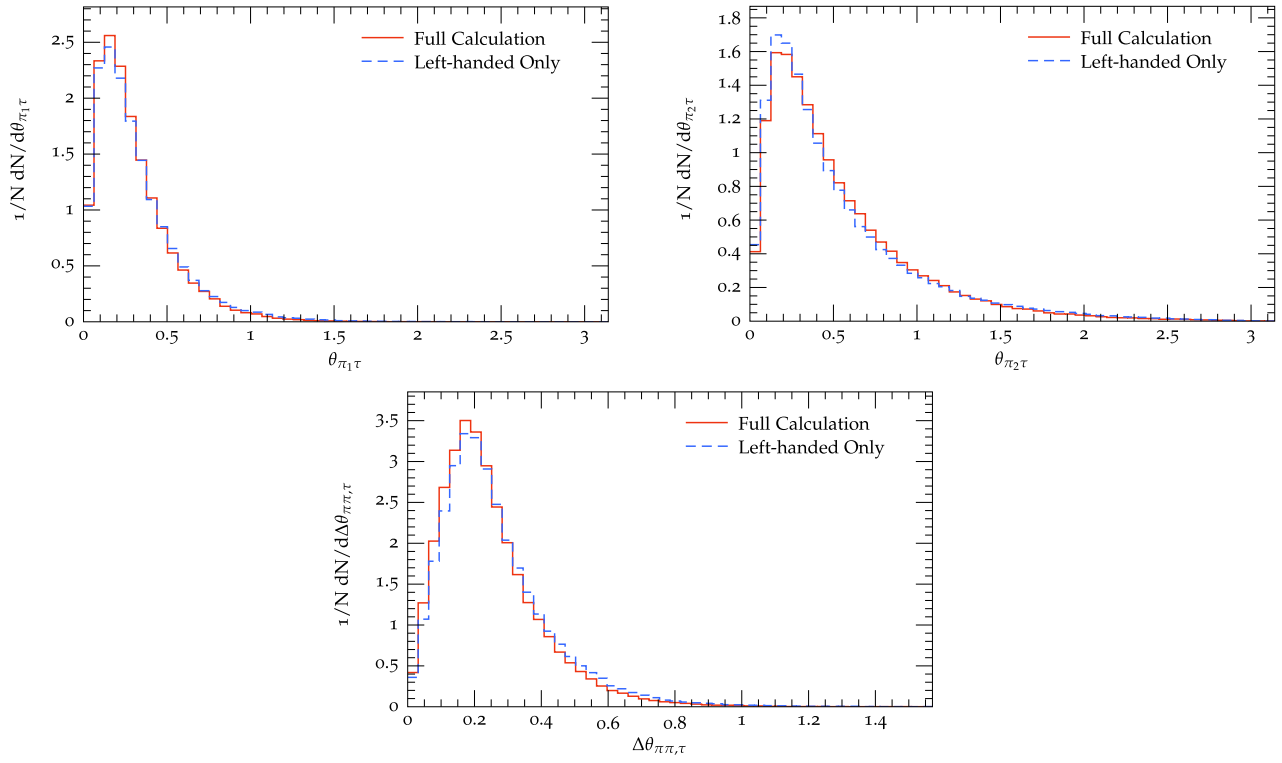


FIG. 21. The distributions of the leading (left) and subleading (right) pion angle with respect to the tau lepton for the decay channel $\tau \to \pi\pi\nu_\tau$ are shown. Additionally, the angle between the two pions and the tau lepton is shown in the bottom. The results with the purely left-handed approximation are given in blue, while the full calculation is given in red.

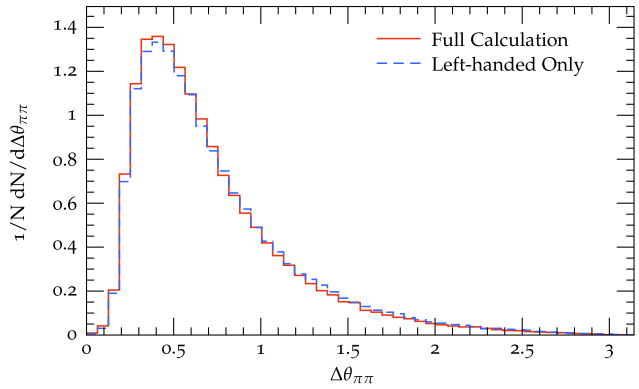


FIG. 22. The distribution of the opening angle between the two pions for the decay channel $\tau \to \pi\pi\nu_\tau$ is shown. The results with the purely left-handed approximation are given in blue, while the full calculation is given in red.

the leading, subleading, and sub-subleading pions are shown. Here we can see no significant impact on the distributions for any of the pions. Additionally, in Figs. 24 and 25, we investigate the effects in the angle of the leading pion, subleading pion, sub-subleading pion, and the three-pion system with respect to the neutrino beam and with respect to the tau lepton respectively. In the aforementioned distributions, the left-hand only and the full calculation have negligible differences. Finally, we consider the opening angle between all possible combinations of pions in Fig. 26, and find no significant impact on the observable from appropriately handling the spin correlations.

In this case, the shift in all the distributions is not very significant. However, there may be higher-dimensional correlations between the observables that can be exploited through the use of tools like machine learning. Obtaining the separation between signal and background and the exact impact of using the full calculation are left to a future work.

### 5. Four-pion distributions

Finally, we investigate the case of events with exactly four pions in the final state, i.e. $\tau \to \pi\pi\pi\pi\nu_\tau$. We consider the same set of observables as in the two- and three-pion cases, but with the additional combinations that can be constructed with four pions. In Fig. 27, the momentum of the leading, subleading, sub-subleading, and sub-sub-subleading pions are shown. Here we can see no significant impact on the distributions for any of the pions. Additionally, in Figs. 28 and 29, we investigate the effects in the angle of the leading pion, subleading pion, sub-subleading pion, sub-sub-subleading pion and the four-pion system with respect to

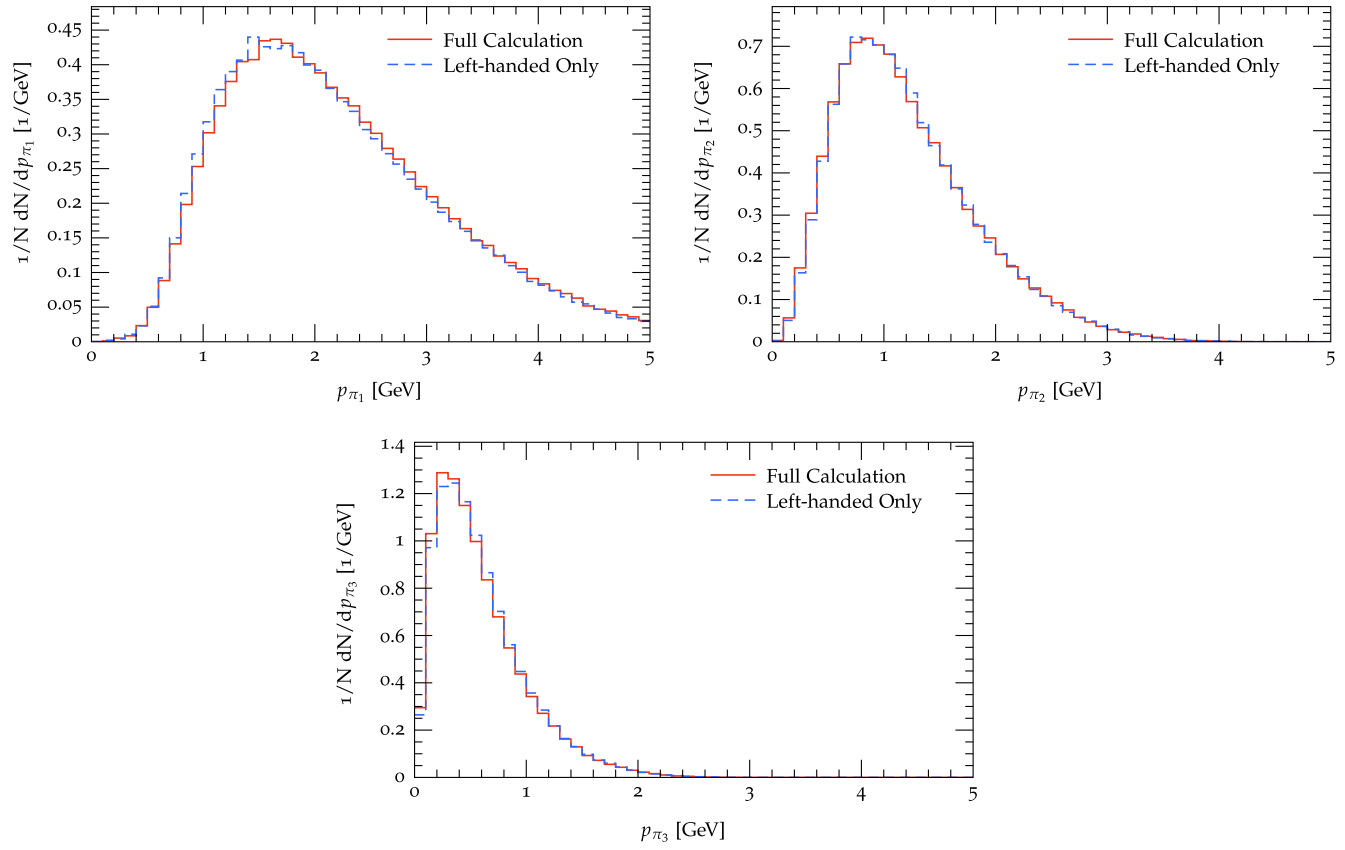


FIG. 23. The distributions of the leading (upper left), subleading (upper right), and sub-subleading (bottom) momentum of the pion for the decay channel $\tau \to \pi\pi\pi\nu_\tau$ are shown. The results with the purely left-handed approximation are given in blue, while the full calculation is given in red.

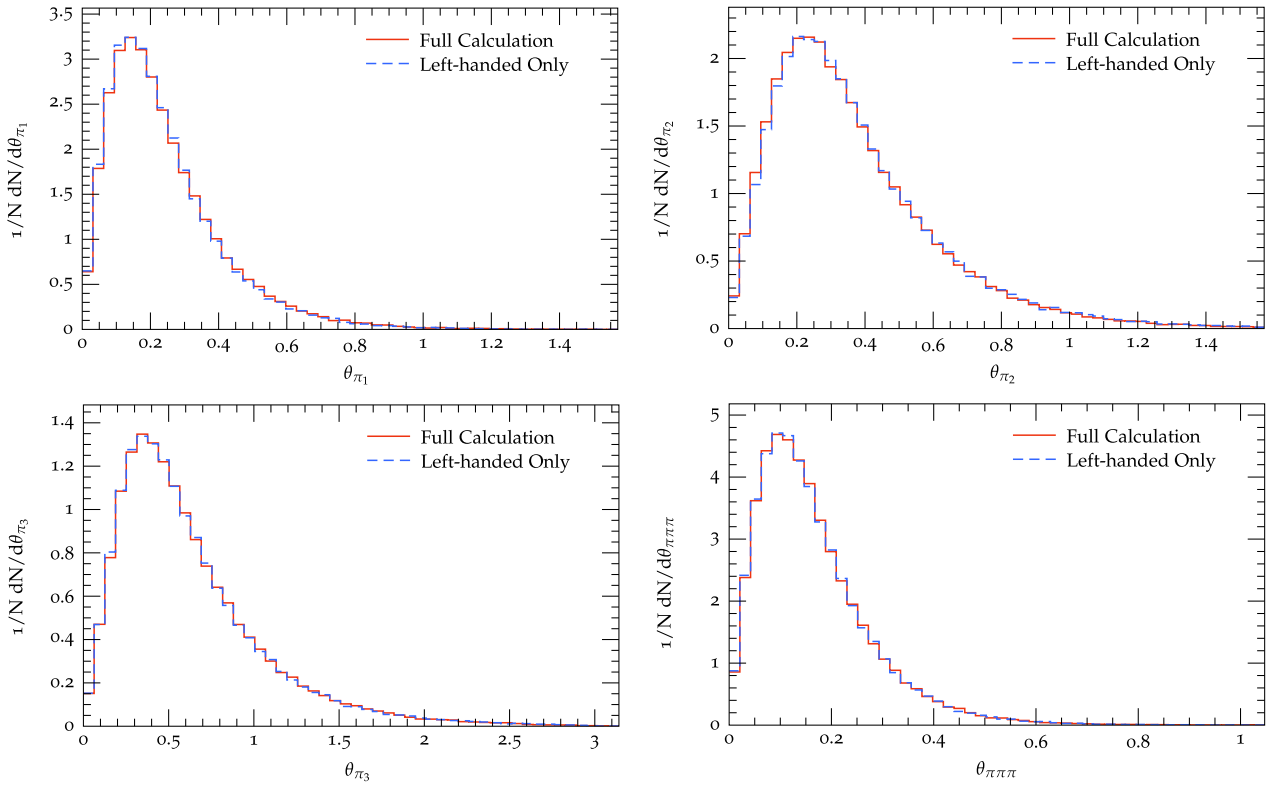


FIG. 24. The distributions of the angle formed by the leading (upper left), subleading (upper right), sub-subleading (bottom left), and three pion system (bottom right) with respect to the neutrino beam axis, respectively, for the decay channel $\tau \to \pi\pi\pi\nu_\tau$ are shown. The results with the purely left-handed approximation are given in blue, while the full calculation is given in red.

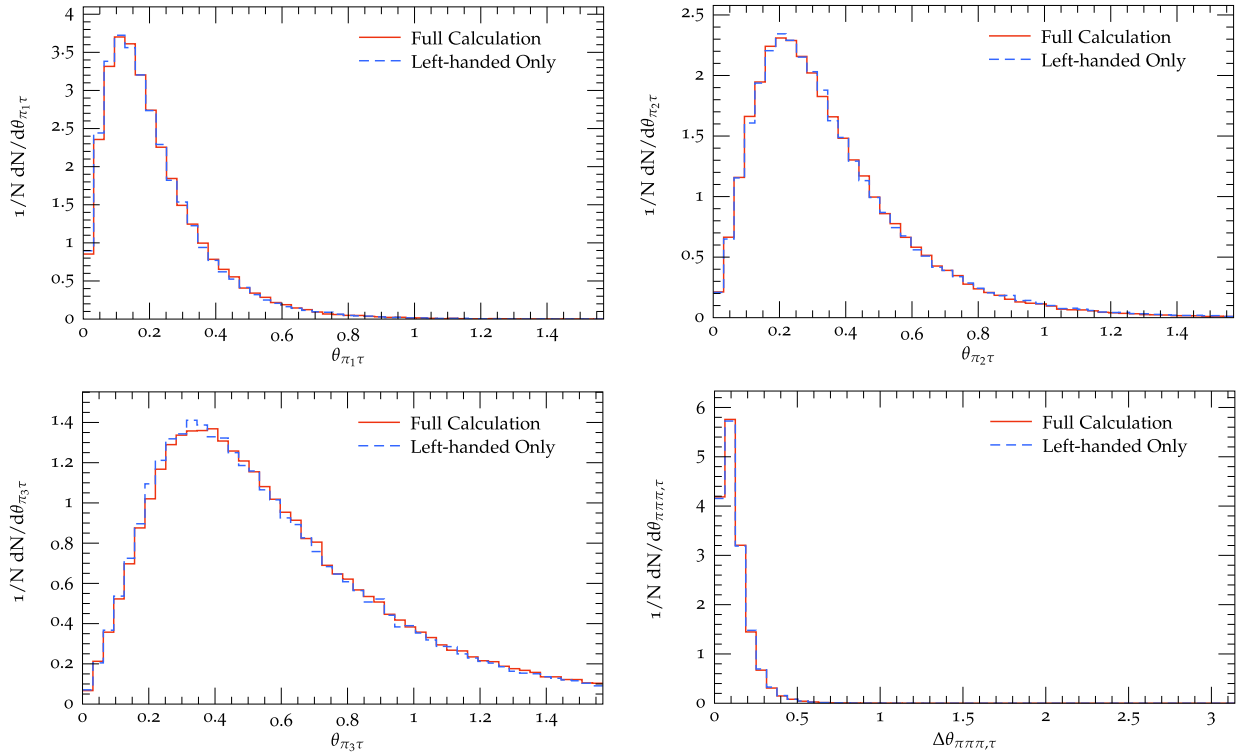


FIG. 25. The distributions of the angle formed by the leading (upper left), subleading (upper right), sub-subleading (bottom left), and three pion system (bottom right) with respect to the tau lepton axis, respectively, for the decay channel $\tau \to \pi\pi\pi\nu_\tau$ are shown. The results with the purely left-handed approximation are given in blue, while the full calculation is given in red.

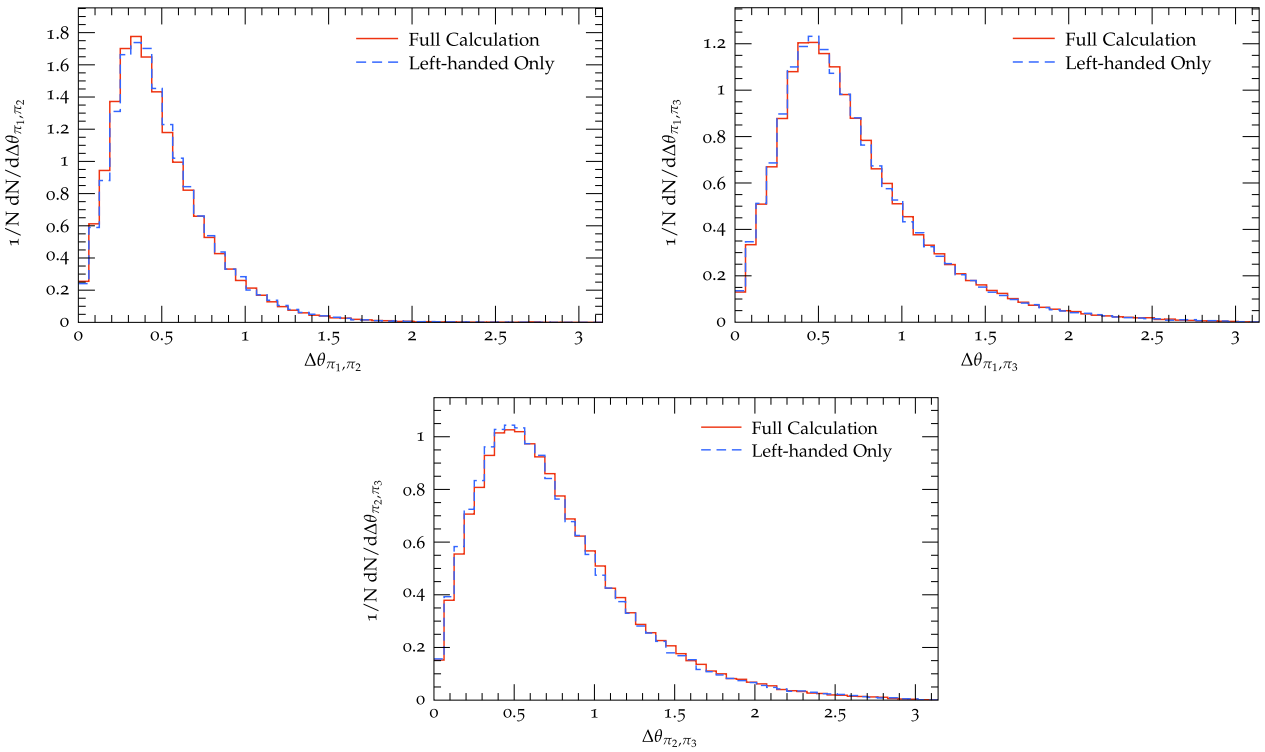


FIG. 26. The distributions of the opening angle formed by the leading and subleading pions (upper left), leading and sub-subleading pions (upper right), and subleading and sub-subleading pions (bottom), for the decay channel $\tau \to \pi\pi\pi\nu_\tau$ are shown. The results with the purely left-handed approximation are given in blue, while the full calculation is given in red.

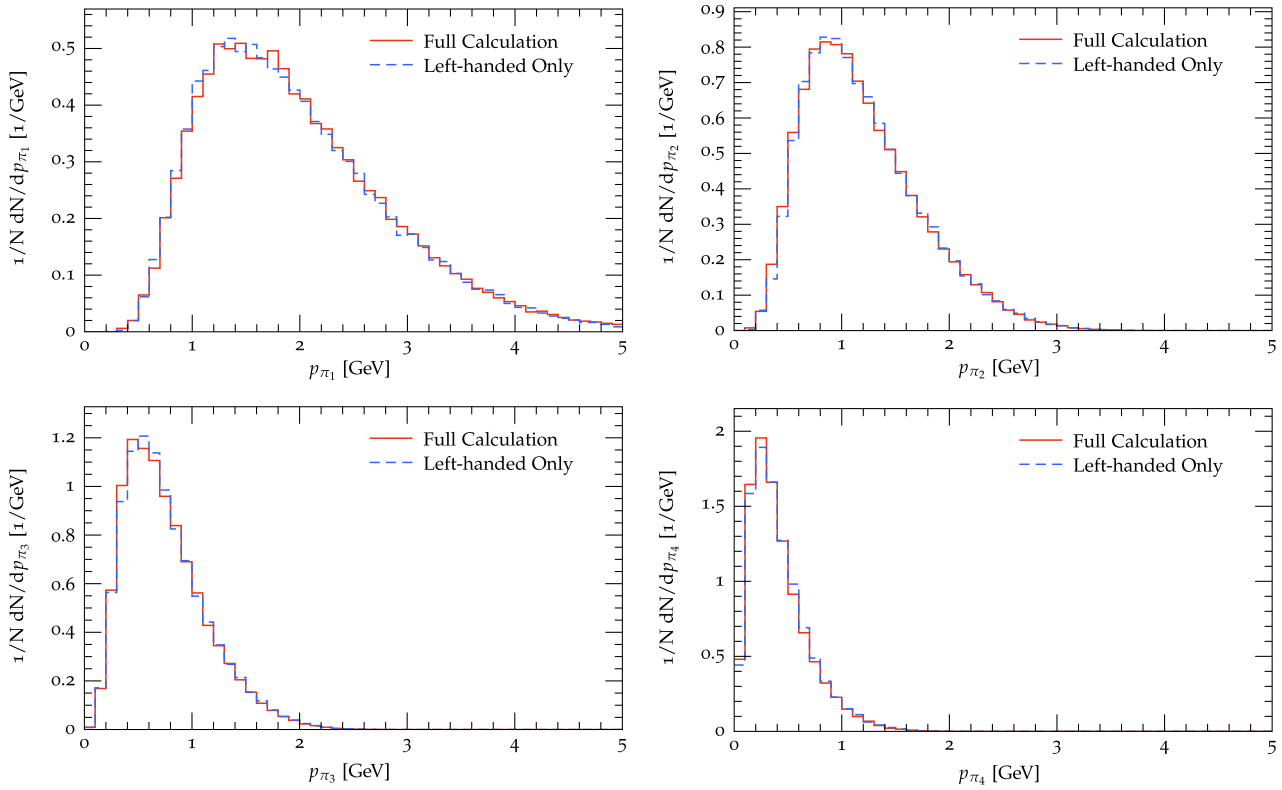


FIG. 27. The distributions of the leading (upper left), subleading (upper right), sub-subleading (bottom left), and subsubsubleading (bottom right) momentum of the pion for the decay channel $\tau \to \pi\pi\pi\pi\nu_\tau$ are shown. The results with the purely left-handed approximation are given in blue, while the full calculation is given in red.

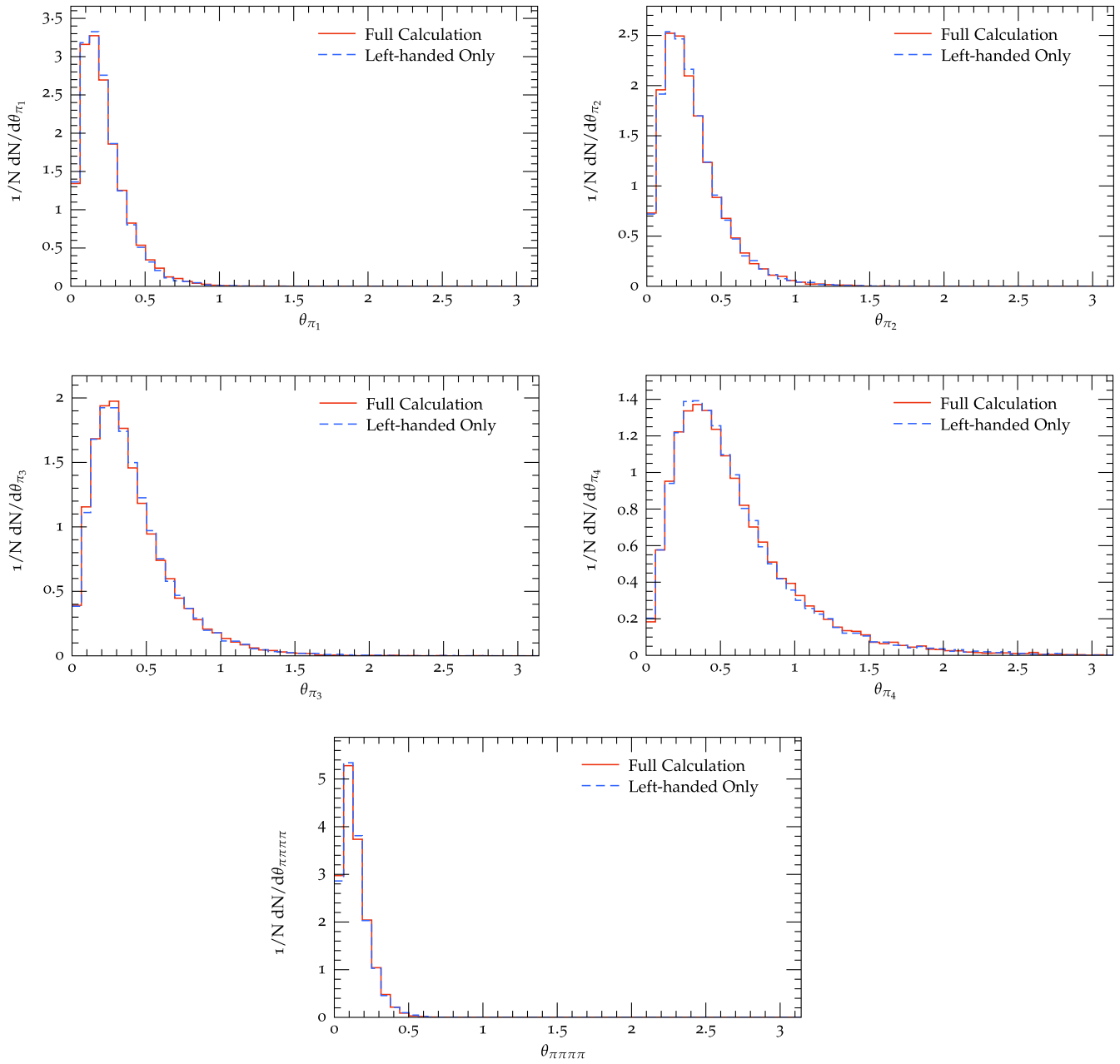


FIG. 28. The distributions of the angle formed by the leading (upper left), subleading (upper right), sub-subleading (middle left), sub-sub-subleading (middle right) and four pion system (bottom) with respect to the neutrino beam axis, respectively, for the decay channel $\tau \to \pi\pi\pi\pi\nu_\tau$ are shown. The results with the purely left-handed approximation are given in blue, while the full calculation is given in red.

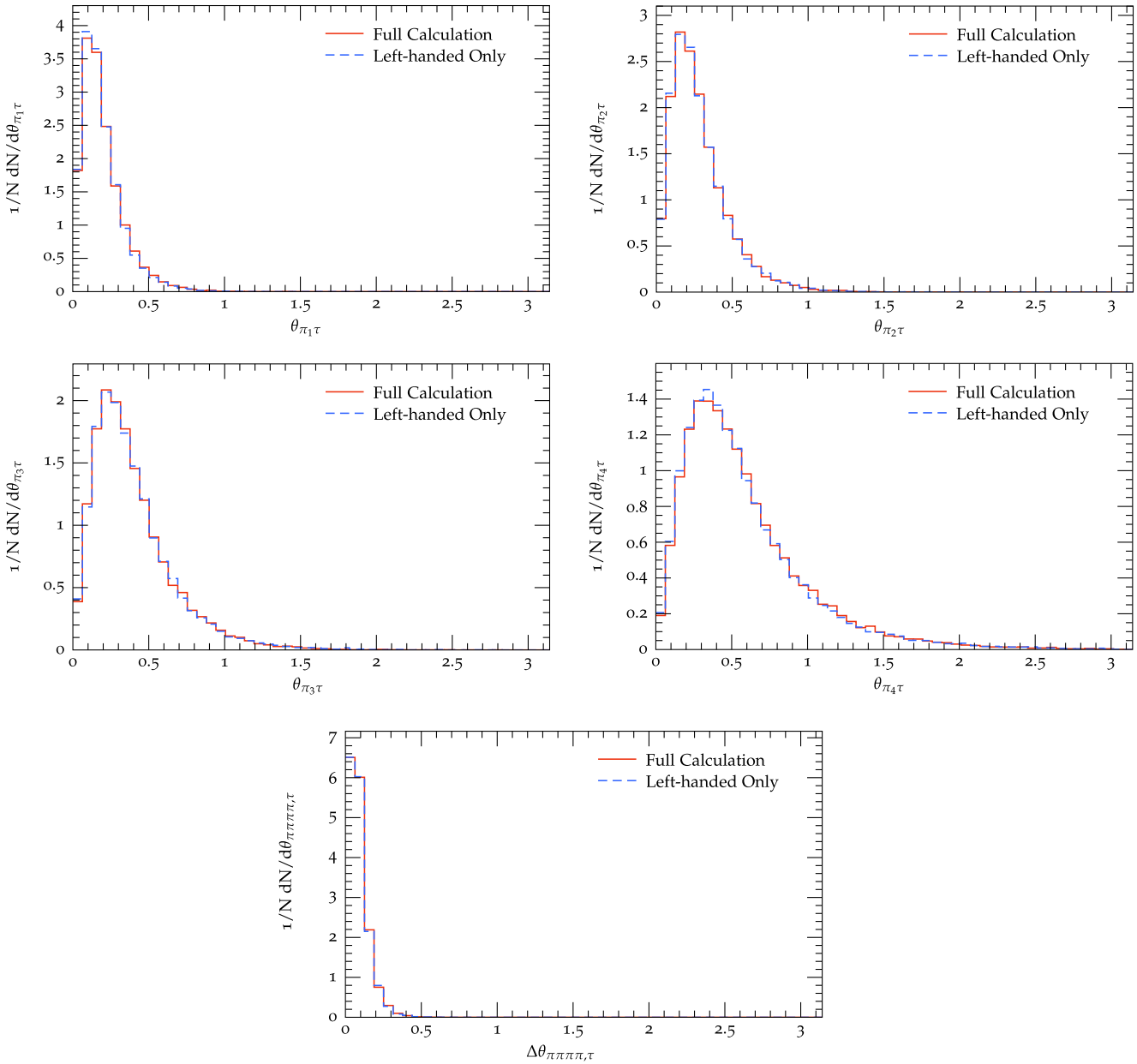


FIG. 29. The distributions of the angle formed by the leading (upper left), subleading (upper right), sub-subleading (middle left), sub-sub-subleading (middle right) and four pion system (bottom) with respect to the tau lepton axis, respectively, for the decay channel $\tau \to \pi\pi\pi\pi\nu_\tau$ are shown. The results with the purely left-handed approximation are given in blue, while the full calculation is given in red.

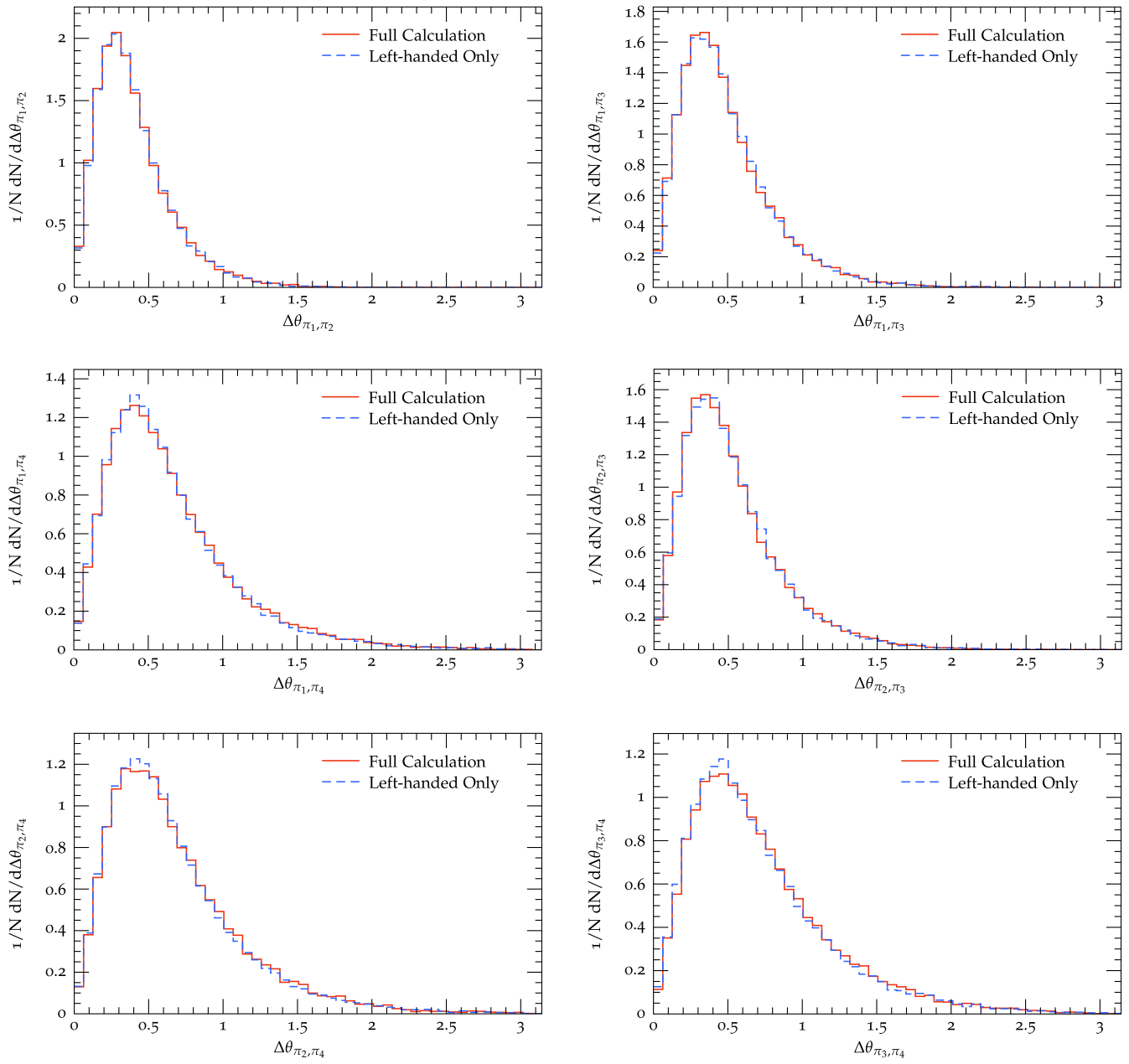


FIG. 30. The distributions of the opening angle formed by the leading and subleading pions (upper left), leading and sub-subleading pions (upper right), leading and sub-sub-subleading pions (middle left), subleading and sub-subleading pions (middle right), subleading and sub-sub-subleading pions (bottom left), and sub-subleading and sub-sub-subleading pions (bottom right), for the decay channel $\tau \to \pi\pi\pi\pi\nu_\tau$ are shown. The results with the purely left-handed approximation are given in blue, while the full calculation is given in red.

the neutrino beam and with respect to the tau lepton respectively. In the aforementioned distributions, the left-hand only and the full calculation have negligible differences. Finally, we consider the opening angle between all possible combinations of pions in Fig. 30, and find no significant impact on the observable from appropriately handling the spin correlations.

In this case, just like the three-pion case, the shift in all the distributions is not very significant. However, higher-dimensional correlations may exist. These correlations may be found through the use of tools like machine learning. Finding the correlations and optimizing the signal vs background selection are left to a future work.

[1] K. Kodama *et al.* (DONuT Collaboration), Phys. Lett. B **504**, 218 (2001).
[2] K. Kodama *et al.* (DONuT Collaboration), Phys. Rev. D **78**, 052002 (2008).
[3] N. Agafonova *et al.* (OPERA Collaboration), Phys. Rev. Lett. **120**, 211801 (2018); **121**, 139901(E) (2018).
[4] Z. Li *et al.* (Super-Kamiokande Collaboration), Phys. Rev. D **98**, 052006 (2018).
[5] M. G. Aartsen *et al.* (IceCube Collaboration), Phys. Rev. D **99**, 032007 (2019).
[6] R. Abbasi *et al.* (IceCube Collaboration), Eur. Phys. J. C **82**, 1031 (2022).
[7] A. De Gouvêa, K. J. Kelly, G. V. Stenico, and P. Pasquini, Phys. Rev. D **100**, 016004 (2019).
[8] B. Abi *et al.* (DUNE Collaboration), arXiv:2002.03005.
[9] A. Ishihara (IceCube Collaboration), Proc. Sci. ICRC2019 (**2021**) 1031 [arXiv:1908.09441].
[10] A. Ghoshal, A. Giarnetti, and D. Meloni, J. High Energy Phys. 12 (2019) 126.
[11] J. L. Feng *et al.*, J. Phys. G **50**, 030501 (2023).
[12] I. Esteban, S. Pandey, V. Brdar, and J. F. Beacom, Phys. Rev. D **104**, 123014 (2021).
[13] C. A. Argüelles, M. Bustamante, A. Kheirandish, S. Palomares-Ruiz, J. Salvado, and A. C. Vincent, Proc. Sci. ICRC2019 (2020) 849 [arXiv:1907.08690].
[14] R. Mammen Abraham *et al.*, J. Phys. G **49**, 110501 (2022).
[15] T. Kosc, Kinematic search for $\tau$ neutrino appearance in the DUNE experiment, Ph.D. thesis, Lyon University, 2021.
[16] J. E. Sobczyk, N. Rocco, and J. Nieves, Phys. Rev. C **100**, 035501 (2019).
[17] E. Hernández, J. Nieves, F. Sánchez, and J. E. Sobczyk, Phys. Lett. B **829**, 137046 (2022).
[18] P. Machado, H. Schulz, and J. Turner, Phys. Rev. D **102**, 053010 (2020).
[19] C. Andreopoulos *et al.*, Nucl. Instrum. Methods Phys. Res., Sect. A **614**, 87 (2010).
[20] T. Golan, J. T. Sobczyk, and J. Zmuda, Nucl. Phys. B, Proc. Suppl. **229–232**, 499 (2012).
[21] Y. Hayato and L. Pickering, Eur. Phys. J. Spec. Top. **230**, 4469 (2021).
[22] T. Leitner, L. Alvarez-Ruso, and U. Mosel, Phys. Rev. C **73**, 065502 (2006).
[23] M. Chrzaszcz, T. Przedzinski, Z. Was, and J. Zaremba, Comput. Phys. Commun. **232**, 220 (2018).
[24] J. Isaacson, W. I. Jay, A. Lovato, P. A. N. Machado, and N. Rocco, Phys. Rev. D **107**, 033007 (2023).
[25] T. Gleisberg, S. Höche, F. Krauss, A. Schälicke, S. Schumann, and J. Winter, J. High Energy Phys. 02 (2004) 056.
[26] T. Gleisberg, S. Höche, F. Krauss, M. Schönherr, S. Schumann, F. Siegert, and J. Winter, J. High Energy Phys. 02 (2009) 007.
[27] E. Bothmann *et al.* (Sherpa Collaboration), SciPost Phys. **7**, 034 (2019).
[28] J. Isaacson, S. Höche, D. Lopez Gutierrez, and N. Rocco, Phys. Rev. D **105**, 096006 (2022).
[29] N. D. Christensen and C. Duhr, Comput. Phys. Commun. **180**, 1614 (2009).
[30] A. Alloul, N. D. Christensen, C. Degrande, C. Duhr, and B. Fuks, Comput. Phys. Commun. **185**, 2250 (2014).
[31] E. A. Paschos and J. Y. Yu, Phys. Rev. D **65**, 033002 (2002).
[32] J. Conrad, A. de Gouvea, S. Shalgar, and J. Spitz, Phys. Rev. D **82**, 093012 (2010).
[33] B. K. Bullock, K. Hagiwara, and A. D. Martin, Nucl. Phys. **B395**, 499 (1993).
[34] A. D. Martin and T. D. Spearman, *Elementary Particle Theory* (North-Holland Publishing Co., Amsterdam, 1970).
[35] M. Valverde, J. E. Amaro, J. Nieves, and C. Maieron, Phys. Lett. B **642**, 218 (2006).
[36] T. Laubrich, Diploma Thesis, TU Dresden, 2006.
[37] F. Siegert, Diploma Thesis, TU Dresden, 2007.
[38] R. L. Workman *et al.* (Particle Data Group), Prog. Theor. Exp. Phys. **2022**, 083C01 (2022).
[39] J. H. Kühn and A. Santamaría, Z. Phys. C **48**, 445 (1990).
[40] G. Ecker, J. Gasser, A. Pich, and E. de Rafael, Nucl. Phys. **B321**, 311 (1989).
[41] P. Richardson, J. High Energy Phys. 11 (2001) 029.
[42] T. Gleisberg and S. Höche, J. High Energy Phys. 12 (2008) 039.
[43] S. Höche, S. Kuttimalai, S. Schumann, and F. Siegert, Eur. Phys. J. C **75**, 135 (2015).
[44] C. Degrande, C. Duhr, B. Fuks, D. Grellscheid, O. Mattelaer, and T. Reiter, Comput. Phys. Commun. **183**, 1201 (2012).
[45] A. Buckley, J. Butterworth, L. Lönnblad, D. Grellscheid, H. Hoeth, L. Lönnblad, J. Monk, H. Schulz, and F. Siegert, Comput. Phys. Commun. **184**, 2803 (2013).
[46] C. Bierlich *et al.*, SciPost Phys. **8**, 026 (2020).
[47] J. Isaacson, S. Hoeche, F. Siegert, and S. Wang, Dune Tau Polarization FD Analysis (1.1), Zenodo, 10.5281/zenodo.8270276.
[48] O. Benhar, A. Fabrocini, S. Fantoni, and I. Sick, Nucl. Phys. **A579**, 493 (1994).
[49] J. J. Kelly, Phys. Rev. C **70**, 068202 (2004).
[50] L. Fields, DUNE fluxes, https://glaucus.crc.nd.edu/DUNEFluxes/.
[51] P. F. de Salas, D. V. Forero, S. Gariazzo, P. Martínez-Miravé, O. Mena, C. A. Ternes, M. Tórtola, and J. W. F. Valle, J. High Energy Phys. 02 (2021) 071.